medRxiv preprint doi: https://doi.org/10.1101/2024.06.27.24309417; this version posted July 1, 2024. The copyright holder for this preprint (which was not certified by peer review) is the author/funder, who has granted medRxiv a license to display the preprint in perpetuity. It is made available under a CC-BY 4.0 International license .

Pathogenic variants in *TMEM184B* cause a neurodevelopmental syndrome via alteration of metabolic signaling

Kimberly A Chapman*[1], Farid Ullah*[2,3], Zachary A Yahiku*[4], Sri Varsha Kodiparthi[5], Georgios Kellaris[2], Sandrina P Correia[6,7], Tommy Stödberg[8], Christalena Sofokleous[9], Nikolaos M Marinakis[9,10], Helena Fryssira[9], Eirini Tsoutsou[9], Jan Traeger-Synodinos[9], Andrea Accogli[11], Vincenzo Salpietro[12,13], Pasquale Striano[14,15], Seth I Berger[1], Kelvin W Pond[16], Suman Sirimulla[5], Erica E Davis[2,3#], Martha RC Bhattacharya[4#]

1: Children's National Rare Disease Institute and Center for Genetic Medicine Research, Washington DC, USA.

2: Stanley Manne Children's Research Institute, Ann & Robert H. Lurie Children's Hospital of Chicago, Chicago, IL, USA.

3: Department of Pediatrics and Department of Cell and Developmental Biology, Feinberg School of Medicine, Northwestern, Chicago, IL, USA.

4: Department of Neuroscience, University of Arizona, Tucson AZ, USA.

5: AIQure LLC, El Paso, TX, USA.

6: Centre for Inherited Metabolic Diseases, Karolinska University Hospital, Stockholm, Sweden.

7: Department of Molecular Medicine and Surgery, Karolinska Institutet, Stockholm, Sweden.

8: Department of Women's and Children`s Health, Karolinska Institute, Stockholm, Sweden; and Department of Pediatric Neurology, Karolinska University Hospital, Stockholm, Sweden.

9: Laboratory of Medical Genetics, Medical School, National and Kapodistrian University of Athens, St. Sophia's Children's Hospital, Athens, Greece.

NOTE: This preprint reports new research that has not been certified by peer review and should not be used to guide clinical practice.

medRxiv preprint doi: https://doi.org/10.1101/2024.06.27.24309417; this version posted July 1, 2024. The copyright holder for this preprint (which was not certified by peer review) is the author/funder, who has granted medRxiv a license to display the preprint in perpetuity. It is made available under a CC-BY 4.0 International license .

10: Research University Institute for the Study and Prevention of Genetic and Malignant Disease of Childhood,National and Kapodistrian University of Athens, St. Sophia's Children's Hospital, Athens, Greece.

11: Division of Medical Genetics, Department of Medicine, and Department of Human Genetics, McGill University, Montreal, QC, Canada.

12: Department of Neuromuscular Disorders, Queen Square Institute of Neurology, University. College London, London, WC1N 3BG, UK.

13: Department of Biotechnological and Applied Clinical Sciences, University of L'Aquila, 67100, L'Aquila, Italy.

14: Department of Neurosciences, Rehabilitation, Ophthalmology, Genetics, Maternal and Child Health (DINOGMI), University of Genoa, Genoa, Italy

15: IRCCS Giannina Gaslini Institute, Genoa, Italy.

16: Department of Cellular and Molecular Medicine, University of Arizona College of Medicine - Tucson, AZ, USA.

*These authors contributed equally.

#Corresponding authors: Erica Davis (eridavis@luriechildrens.org), Martha Bhattacharya (marthab1@arizona.edu)

medRxiv preprint doi: https://doi.org/10.1101/2024.06.27.24309417; this version posted July 1, 2024. The copyright holder for this preprint (which was not certified by peer review) is the author/funder, who has granted medRxiv a license to display the preprint in perpetuity. It is made available under a CC-BY 4.0 International license .

ABSTRACT:

Transmembrane protein 184B (TMEM184B) is an endosomal 7-pass transmembrane protein with evolutionarily conserved roles in synaptic structure and axon degeneration. We report six pediatric patients who have *de novo* heterozygous variants in *TMEM184B*. All individuals harbor rare missense or mRNA splicing changes and have neurodevelopmental deficits including intellectual disability, corpus callosum hypoplasia, seizures, and/or microcephaly. TMEM184B is predicted to contain a pore domain, wherein many human disease-associated variants cluster. Structural modeling suggests that all missense variants alter TMEM184B protein stability. To understand the contribution of TMEM184B to neural development *in vivo*, we suppressed the TMEM184B ortholog in zebrafish and observed microcephaly and reduced anterior commissural neurons, aligning with patient symptoms. Ectopic *TMEM184B* expression resulted in dominant effects for K184E and G162R. However, *in vivo* complementation studies demonstrate that all other variants tested result in diminished protein function and indicate a haploinsufficiency basis for disease. Expression of K184E and other variants increased apoptosis in cell lines and altered nuclear localization of transcription factor EB (TFEB), a master regulator of lysosomal biogenesis, suggesting disrupted nutrient signaling pathways. Together, our data indicate that TMEM184B variants cause cellular metabolic disruption likely through divergent molecular effects that all result in abnormal neural development.

medRxiv preprint doi: https://doi.org/10.1101/2024.06.27.24309417; this version posted July 1, 2024. The copyright holder for this preprint (which was not certified by peer review) is the author/funder, who has granted medRxiv a license to display the preprint in perpetuity. It is made available under a CC-BY 4.0 International license .

INTRODUCTION

Transmembrane protein 184B (TMEM184B) is an endosomal transmembrane protein that facilitates synaptic maintenance and axon degeneration across species. Loss of TMEM184B in mouse and *Drosophila* models causes synaptic malformations and neuronal hyperactivity.[1–3] While these studies highlight an important role for TMEM184B in the maintenance of nervous system integrity in adult organisms, its role in the processes required for neural development remain less clear. Primary embryonic sensory neurons from mice with a mutation in *Tmem184b* (gene trap model) show a reduction in transcripts related to Wnt signaling, a classical developmental pathway with substantial nervous system effects.[3–5] Given the broad expression of *TMEM184B* in the central nervous system[6] coupled with the effects of its loss on the Wnt signaling pathway, it is hypothesized that TMEM184B function may contribute to neuronal differentiation, migration, and/or survival. However, the neurodevelopmental disruptions that result from *TMEM184B* impairment are unknown.

Few studies have examined the effects of TMEM184B alteration in human cells. Knockdown of *TMEM184B* in carcinoma cell lines causes reduced proliferation *in vitro* and in tumor xenografts, suggesting that its function is critical for the growth of malignant cells.[7] TMEM184B transcripts are upregulated in squamous cell carcinoma clinical samples and have been implicated in increased metastatic cell migration via regulation of the cytoskeleton.[8] Finally, genome-wide association studies have implicated TMEM184B in mammographic density-associated breast cancer risk.[9] Together, these studies suggest a link between TMEM184B expression and cellular growth and survival. Recently a large-scale Mendelian disease sequencing effort proposed *TMEM184B* as a candidate gene; a single individual with corpus callosum hypoplasia and seizures was reported to have a de novo *TMEM184B* variant, though the precise DNA change and other clinical

medRxiv preprint doi: https://doi.org/10.1101/2024.06.27.24309417; this version posted July 1, 2024. The copyright holder for this preprint (which was not certified by peer review) is the author/funder, who has granted medRxiv a license to display the preprint in perpetuity. It is made available under a CC-BY 4.0 International license .

information was not given.[10] Aside from this case, pathogenic variants in this gene have not been described or studied in human populations.

During development, alteration of cellular proliferation and growth signaling pathways can have devastating consequences, especially for the central nervous system which grows dramatically in the final trimester of human gestation.[11,12] Two of the most common neurological diagnoses in children are corpus callosum dysgenesis and seizures. These diagnoses often co-occur in patients, suggesting that the affected processes may be molecularly or functionally related. Microcephaly is a severe presentation of neurodevelopmental growth disruption that is defined by smaller average head circumference (when controlled for other factors) and can have either environmental or genetic causes. Recent work has used exome and genome sequencing approaches to characterize potential causal gene variants, resulting in a group of genes implicated in the process.[13] Unsurprisingly, these genes cluster in pathways known to affect axon outgrowth (e.g. tubulin isoforms TUBA1A, TUBB3) and neuronal differentiation (CTNNB1, FOXG1).

Neurons and neural progenitors require cellular sensors to detect nutrient status to make decisions about growth and differentiation. Transcription factor EB (TFEB) acts as a key regulator of lysosomal and autophagosomal gene transcription, and its localization is acutely sensitive to cellular amino acid levels. In high nutrient conditions, TFEB is phosphorylated by multiple kinases that regulate cell growth including the mechanistic target of rapamycin C1 (mTORC1) complex and mitogen activated protein kinase 4K3 (MAP4K3).[14] Phosphorylation sequesters TFEB in the cytoplasm via its interaction with 14-3-3 protein and prevents its transcriptional activities.[15] Upon starvation, both mTORC1 and MAPK pathways are inhibited, TFEB becomes dephosphorylated, and it enters the nucleus where it binds to a defined enhancer (called the CLEAR motif) and promotes transcription of mRNAs encoding autophagosomal and lysosomal components.[16] By promoting the formation of additional autophagosomes and lysosomes, TFEB

medRxiv preprint doi: https://doi.org/10.1101/2024.06.27.24309417; this version posted July 1, 2024. The copyright holder for this preprint (which was not certified by peer review) is the author/funder, who has granted medRxiv a license to display the preprint in perpetuity. It is made available under a CC-BY 4.0 International license .

transcriptional activity increases cellular catabolism to promote short-term survival. TFEB exits the nucleus when nutrient levels have been restored to baseline via degradation of cellular proteins.[17] TFEB nuclear-cytoplasmic shuttling dynamics are altered in neurological diseases. Aberrant accumulation of TFEB in the nucleus occurs in lysosomal storage disorders, which are childhood-onset diseases caused by improper lysosomal cargo degradation.[16] On the other hand, TFEB nuclear entry is reduced in the most common genetic type of amyotrophic lateral sclerosis (ALS) caused by repeat expansion in the *C9ORF72* locus.[18] Therefore, promoting TFEB transcriptional activity is being explored as one avenue to treat neurodegenerative disorders by promoting degradation of misfolded proteins and malfunctioning organelles.

Here we describe the identification of a cohort of affected individuals with *de novo*, heterozygous variants in *TMEM184B*. These variants afford us an opportunity to gain insight into the structural features of the protein, the molecular function of TMEM184B, and the consequences to human health. We use zebrafish to implicate the TMEM184B ortholog in animal growth, development of anterior structures and emanation of commissural neurons. We test both dominant and loss of function variant hypotheses *in vivo* and show that disease-associated variants can have diverse molecular effects. Further, we find variant-dependent effects on TFEB nuclear localization, suggesting a pathological explanation for the effects of patient variants on cellular function and neural development. Our work highlights a new cause of neurodevelopmental disorders and provides critical insight into the rare syndrome caused by *TMEM184B* disruption.

MATERIALS/METHODS:

Patient Inclusion

All research was performed in accordance with the Declaration of Helsinki. Most participants were identified by clinical sequencing and then unified via GeneMatcher.[19]

medRxiv preprint doi: https://doi.org/10.1101/2024.06.27.24309417; this version posted July 1, 2024. The copyright holder for this preprint (which was not certified by peer review) is the author/funder, who has granted medRxiv a license to display the preprint in perpetuity. It is made available under a CC-BY 4.0 International license .

Subjects and their families agreed to allow de-identified information to be summarized from medical chart review and reported in this study. Subject 5 was also consented for fibroblast utilization and maintenance to a biorepository, which allows for residual samples from clinical procedures be collected, saved and distributed for research.

Genome Sequencing and Analysis

Sequencing was performed at each institution using either genome or exome approaches. Allele frequency was estimated using data from the gnomAD database (version 4.1.0) (https://gnomad.broadinstitute.org/) and was last queried in May 2024. Alphamissense was used to evaluate possible pathogenicity of each missense variant.[20] All analyses of sequence variation used transcript NM_001195071.1.

Structure Prediction

The native protein sequence was extracted from Uniprot, and each variant was inserted accordingly. Alphafold, along with MMSeq2, was employed to generate 3D structures of TMEM184B and its five clinically relevant missense variants. Structures were quality assessed via PLDDT and PAE scores, which provided five models for each protein structure. PLDDT gives the confidence score of the structure predicted (the higher, the better). Some loop regions that did not fit the desired criteria were truncated for cross-validation of the results. To assess the quality and reliability of the predicted protein geometry, the backbone dihedral angles of the predicted protein structures were mapped onto a Ramachandran plot. Similar to the PLDDT plot, we truncated the protein structure at the membrane to remove sequences in loops, a common practice in structural biology.[21] Visualizations, including overlays of native and variant predicted protein structures, were created in Pymol 2.6. The best structure for native protein was chosen based on the highest PLDDT scores and the most favorable Ramachandran plot.

Zebrafish Husbandry and Embryo Maintenance

medRxiv preprint doi: https://doi.org/10.1101/2024.06.27.24309417; this version posted July 1, 2024. The copyright holder for this preprint (which was not certified by peer review) is the author/funder, who has granted medRxiv a license to display the preprint in perpetuity. It is made available under a CC-BY 4.0 International license .

All experimental procedures were performed according to protocols approved by the Northwestern University Institutional Animal Care and Use Committee (IACUC; Protocol IS00016405). Wild type (WT) AB adults were maintained in standard husbandry conditions on a 14h light and 10h dark cycle. Embryos were obtained from natural matings with a 14 day rest period between each mating. Embryos were grown in egg water (0.3 g/L NaCl, 75 mg/L $CaSO_4$, 37.5 mg/L $NaHC0_3$, 0.003% methylene blue) at 28.5°C until phenotypic readout or tissue harvest.

Transient Depletion of *tmem184ba*

We obtained a morpholino (MO) to target the splice donor site of *tmem184ba* exon 6 (e6i6), (Gene Tools). *tmem184ba* was suppressed transiently by injecting 1 nl MO at increasing doses (1 ng, 2 ng and 3 ng) into one to four cell staged zebrafish embryos. To determine MO efficiency, we extracted total RNA from pools of 20 larvae/condition (controls and MO-injected) at 2 days post-fertilization (dpf) using Trizol (Thermo Fisher Scientific) according to manufacturer's instructions. cDNA was synthesized with the QuantiTect Reverse Transcription kit (Qiagen). RT-PCR was performed using primers flanking the MO target locus, and amplified PCR products were separated on a 1% agarose gel. The resulting PCR bands were gel purified with the QIAquick gel extraction kit (Qiagen) and cloned into TOPO-TA cloning vector (Thermo Fisher Scientific). The purified plasmids from resulting colonies (n=4/PCR product) were sequenced using BigDye 3.1 terminator chemistry on an ABI3730 Genome Analyzer according to standard protocols.

Molecular Cloning, Site Directed Mutagenesis, and *In Vitro* Transcription of *TMEM184B*

To express human *TMEM184B* WT and variant mRNAs in zebrafish embryos, we obtained a Gateway-compatible WT *TMEM184B* (NM_012264.5; cat# HOC18517) open reading frame (ORF) entry vector (GeneCopoeia). We shuttled the ORF into a pCS2+ Gateway destination

medRxiv preprint doi: https://doi.org/10.1101/2024.06.27.24309417; this version posted July 1, 2024. The copyright holder for this preprint (which was not certified by peer review) is the author/funder, who has granted medRxiv a license to display the preprint in perpetuity. It is made available under a CC-BY 4.0 International license .

vector using LR clonase II (Thermo Fisher Scientific). The *TMEM184B* missense variants identified in affected individuals (V88M, L127R, G162R, K184E, and G288A; or a presumed benign negative control variant (R282H) dbSNP: rs370107940; 215 heterozygous and 4 homozygotes are present in 1609748 individuals in gnomAD v4.1.0) were introduced in the pCS2+ constructs using site-directed mutagenesis as described.[22] After sequence verification of WT and variant ORFs, we linearized each construct with *Not*I and performed *in vitro* transcription with the mMessage mMachine SP6 Transcription kit (Thermo Fisher Scientific) according to manufacturer's instructions. To test dominant effects, we injected 200 pg of each *TMEM184B* mRNA alone, and for a subset of variant mRNAs, titrated with WT in variable doses of 50 pg, 100 pg, and 150 pg while maintaining a total mRNA concentration of 200 pg. For *in vivo* complementation studies to test loss-of-function effects, we injected 200 pg mRNA with 3 ng MO.

Automated Live Imaging of Zebrafish Larvae

To assess head and body size, tricaine-anesthetized larvae were imaged at 3 dpf using the Vertebrate Automated Screening Technology (VAST) Bioimager (Union Biometrica) mounted to an AXIO Imager.M2m microscope (Zeiss) with a 10x objective lens. Larvae were passed sequentially through a 600 mm capillary on the stage module. Each larva was detected by VAST software (version 1.2.6.7) with a 40-70% minimum similarity and oriented automatically using preset recognition templates while operating in automatic imaging mode as described.[23] Bright field lateral and ventral images were captured with the VAST onboard camera.

Whole Mount Immunostaining

Larvae were reared to 3 dpf and fixed overnight in Dent's solution (40% methanol [MeOH] plus 20% dimethyl sulfoxide [DMSO]). Embryos were then rehydrated gradually in MeOH, Phosphate-Buffered Saline (PBS) and 0.1% Tween (T) [PBST] at room temperature. We

medRxiv preprint doi: https://doi.org/10.1101/2024.06.27.24309417; this version posted July 1, 2024. The copyright holder for this preprint (which was not certified by peer review) is the author/funder, who has granted medRxiv a license to display the preprint in perpetuity. It is made available under a CC-BY 4.0 International license .

washed the embryos with bleach solution (9 mL PBST + 1 mL H_2O_2 + 0.05g KOH) for 13 minutes followed by proteinase K treatment for 10 minutes and fixed them in 4% paraformaldehyde (PFA) for 20 minutes at room temperature. Embryos were washed with PBST 3X (10 min each) and incubated in blocking solution (IF buffer [1% BSA in PBST] +10% fetal bovine serum [FBS]) for one to two hours. Primary detection was performed with anti-acetylated tubulin antibody (Sigma-Aldrich, T7451, 1:1,000 overnight at 4º C) and secondary detection with Alexa Fluor 488 goat anti-mouse IgG (Invitrogen; A11001, 1:1,000). Larvae were imaged by capturing fluorescent signal with an AZ100 microscope (Nikon) with a 10X objective mediated by Digital Sight black and white camera (Nikon) and NIS Elements software (Nikon).

Zebrafish Image Analysis

We used ImageJ (NIH) software to measure head and body size from lateral bright field images of zebrafish larvae using consistent anatomical landmarks. For fluorescence images, we measured size of the optic tecta and counted the number of commissural neurons that cross the midline on dorsal images.

Statistical Analysis of Zebrafish Morphometrics

All quantitative data were analyzed with an unpaired student's t-test using GraphPad prism version 8. P-values <0.05 were considered statistically significant. Experiments were performed at least twice with investigator masked to injection conditions.

RT-PCR of *TMEM184B*

Fibroblasts were collected from Patient 5 under IRB-approved procedures. Fibroblasts were converted to induced pluripotent stem cells (iPSC) by the Washington University in St. Louis Genome Engineering and iPSC Center (GEiC). Control iPSC from an unaffected,

medRxiv preprint doi: https://doi.org/10.1101/2024.06.27.24309417; this version posted July 1, 2024. The copyright holder for this preprint (which was not certified by peer review) is the author/funder, who has granted medRxiv a license to display the preprint in perpetuity. It is made available under a CC-BY 4.0 International license .

sex-matched and approximately age-matched individual were purchased from Coriell Biobank (line GM23476). Cells were maintained in mTeSR media (StemCell Technologies) with antibiotics. RNA was isolated using the RNeasy Mini kit (Qiagen). Reverse transcription was performed using the Quanta Bio First Strand Synthesis kit, and PCR was done using Pfusion polymerase (New England Biolabs) according to product recommendations. Primer sequences were as follows: Forward (5'-TGTGTGGTGAAGCCACTCAT-3') and Reverse (5'-ATAAGCCTTGCTCCCAGTGT-3'). Following gel isolation of PCR products, sequencing was submitted to Eton Biosciences (San Diego, CA). Alignments were performed in Snapgene.

Cell Culture and Reporter Cell Line Creation

HEK293T cell lines were cultured in 1X Dulbecco's Modified Eagle Medium (Ref#11995-065) supplemented with 10% FBS, L-glutamine, and 1X Penicillin Streptomycin at 37°C and 5% CO2. To create stable cell lines expressing both TFEB-sfGFP and H2B-mRuby, infection and selection were done sequentially. First, retrovirus expressing TFEB-sfGFP (Addgene Plasmid #135402) was produced by transfecting HEK293T cells with TFEB-GFP plasmid, pVSV-G, and pMD2.G with GeneJuice (Millipore Sigma) and Optimem (Gibco). HEK293T cells were infected with TFEB-sfGFP retrovirus along with polybrene (8ug/mL). A population with high green fluorescence levels was isolated via flow cytometry (BD FACSAria III). TFEB-sfGFP expressing cells were then infected with H2B-mRuby lentivirus (Addgene Plasmid #90236) prepared as above except that VSV-G was replaced with PSPAX2. A population with high TFEB-sfGFP and H2B-mRuby were isolated using FACS and were further selected via sequential treatment with 8 μg/mL puromycin and 400 μg/mL hygromycin.

TFEB Translocation Assay

medRxiv preprint doi: https://doi.org/10.1101/2024.06.27.24309417; this version posted July 1, 2024. The copyright holder for this preprint (which was not certified by peer review) is the author/funder, who has granted medRxiv a license to display the preprint in perpetuity. It is made available under a CC-BY 4.0 International license .

FL-TMEM184B-miRFP670 plasmid constructs were ordered from Twist Bioscience. Plasmid purity and quantity was assessed via Nanodrop (260/280 ratio > 1.9). On Day 0, TFEB-sfGFP/ H2B-mRuby stable cells were transiently transfected with TMEM184B constructs using GeneJuice. On Day 1, each condition was seeded in duplicate into 96-well black bottom plates and transferred to the University of Arizona's Microscope Shared Resource facility and left overnight in 37°C and 5% CO2. On Day 2, media was changed to phenol red-free imaging media. Dulbecco's Modified Eagle Medium (Ref#21063-029) was supplemented with 10% FBS, L-glutamine, 1X Penicillin Streptomycin, and 110 ng/L sodium pyruvate and applied to one duplicate (complete media, non-starved), and Dulbecco's Modified Eagle Medium (Ref#A14430-01) was supplemented with only 1X Penicillin Streptomycin for the other duplicate (starved).

The University of Arizona Microscopy Shared Resource facility's Nikon SoRa spinning-disk confocal microscope was used for imaging. Cells were imaged at 37°C and 5% CO2 in a 4x4 grid with 8% overlap from the center of the well every hour for 6 hours. 20x magnification, 4x4 binning, and 16-bit parameters were used. sfGFP, mRuby, and miRFP670 fluorescent channels were captured.

Image Analysis

A rolling ball background subtraction of 29.86 μm was applied to the sfGFP channel in Nikon NIS Elements software post-acquisition. Individual frames were then exported and analyzed using QuPath imaging pipelines. Cell nuclei were defined by the H2B-mRuby channel and were expanded 2 μm outwards to define the perinuclear region. Detections were filtered through thresholding for nuclear circularity, nuclear area, cell area, GFP intensity, cell circularity, and miRFP670 intensity.

Nuclear to perinuclear sfGFP fluorescence ratios were quantified in non-starved cells, and cells starved at 1-hour and 6-hour timepoints. All conditions were normalized to

medRxiv preprint doi: https://doi.org/10.1101/2024.06.27.24309417; this version posted July 1, 2024. The copyright holder for this preprint (which was not certified by peer review) is the author/funder, who has granted medRxiv a license to display the preprint in perpetuity. It is made available under a CC-BY 4.0 International license .

non-starved HEK293T cells expressing WT TMEM184B. GraphPad Prism 10 was used for statistical analysis. Data normality was assessed using Shapiro-Wilk tests. Nonparametric One-Way ANOVA tests with adjusted p-values were calculated in Graphpad Prism 10, comparing each condition to WT at each timepoint.

Zombie-Violet cell death assay

HEK293T cells were transfected with TMEM184B-miRFP670 containing native sequence or patient variants and cultured for 2 days. Prior to Zombie-Violet assay, cells were starved by incubating with Dulbecco's Modified Eagle Medium (Ref#A14430-01) at 37°C and 5% CO2 for 6 hours. Cell incubation was according to the manufacturer's protocol (BioLegend). Zombie-Violet was diluted 1:500 in DPBS and 100 μL of solution were used per one million cells. Cells were washed with 0.5% BSA/PBS, fixed in 2% PFA, washed once with DPBS, and transferred to the University of Arizona's Flow Cytometry Core to be analyzed (BD FACSCanto II). FlowJo software was used for FACS analysis, and GraphPad Prism 10 was used to create graphs of cell percentages and perform statistical testing (One-Way Parametric ANOVA).

RESULTS

De Novo Heterozygous Disruptions in Human TMEM184B Cause Neurodevelopmental Defects

We leveraged the GeneMatcher platform to identify *TMEM184B* variants that may be disease-causing. We identified six affected individuals in which exome or genome sequencing (ES or GS, respectively) identified a rare mRNA splice site or amino acid disruption to TMEM184B. Subjects and their families agreed to allow de-identified information to be summarized and published in this manuscript. For these patients, we obtained information from physicians and genetic counselors about the alteration in the

medRxiv preprint doi: https://doi.org/10.1101/2024.06.27.24309417; this version posted July 1, 2024. The copyright holder for this preprint (which was not certified by peer review) is the author/funder, who has granted medRxiv a license to display the preprint in perpetuity. It is made available under a CC-BY 4.0 International license .

DNA sequence and the clinical findings observed (**Table 1 and Supplementary Files 1 and 2**). In this dataset, all six affected individuals were diagnosed with neurodevelopmental deficits as children and then, by sequencing, were found to carry a variant of unknown significance (VUS) in the *TMEM184B* locus.

All six patients show phenotypic overlap. Patient symptoms coalesce around a few major clinical findings: developmental delay (5 of 6), corpus callosum hypoplasia (4 of 6, **Figure 1**) or more severe structural disruption resulting in microcephaly (1 of 6), seizures (3 of 6), and intellectual disability (2 of 6). Other non-neurological features are also present in some patients (**Supplemental File 2**). While two patients showed variants of unknown significance (VUS) outside the *TMEM184B* locus, ES or GS of the remaining four patients did not identify other possible genetic contributors to their clinical sequelae. The similarity in presentation across the case series is consistent with a potential causal role for the *TMEM184B* variants in these symptoms. Of note, while our study was ongoing, the V88M variant was reported in gnomAD to be present at a low frequency in the general population (**Table 1**). All missense variants in our study are predicted to be highly damaging to conserved protein structural features, as determined using AlphaMissense (**Table 1**).[20]

Human Variants are Predicted to Alter Structure and Stability of TMEM184B Protein

The *TMEM184B* locus is predicted to be transcribed in two major isoforms, with variant “a” (NM_001195071.1) representing the full sequence. By mapping patient variants onto the linear mRNA, we found that variants cluster in portions of the gene that encode the transmembrane (TM) regions or the loop region between TM3 and TM4 (which is predicted to be cytoplasmic) (**Figure 2A**). We note that the variants within membrane-spanning helices correspond to the most severe patient presentations, suggesting that these changes might be severely disruptive to protein function. The 3D structure of the native protein was predicted using AlphaFold, and the best model was selected based on the

medRxiv preprint doi: https://doi.org/10.1101/2024.06.27.24309417; this version posted July 1, 2024. The copyright holder for this preprint (which was not certified by peer review) is the author/funder, who has granted medRxiv a license to display the preprint in perpetuity. It is made available under a CC-BY 4.0 International license .

PLDDT scores and Ramachandran plot (**Figure 2B-D**). The Ramachandran plot shows the backbone dihedral angles in permitted regions, suggesting a high-quality structure. Figure 2D shows the transmembrane portions of TMEM184B predicted by this model, highlighting the 7 transmembrane domains found in the structure. We then built variants into this model and visualized their effects on the predicted structure (**Figure 2E-F**). Variants V88M and K184E show major disruptions to their transmembrane regions, with large shifts apparent both from top and side views.

We undertook a quantitative analysis of protein structural stability of human TMEM184B using FoldX. The 3-D structures were used as input data for the Mac version of FoldX 5.0 to predict their ΔG. The stability of the protein structures was predicted using FoldX, where the native protein and each variant (G162R, G288A, K184E, L127R, V88M) underwent a stability analysis to calculate their respective total energies. We also performed this analysis for a commonly occurring TMEM184B sequence variant, R282H, as a comparison. The change in Gibbs free energy (ΔΔG) was then determined for each variant relative to the native structure to assess the impact of the mutations on protein stability. Variants with large positive ΔΔG values were associated with destabilizing variants, potentially leading to loss of function, while negative ΔΔG values suggested stabilizing mutations that could result in gain of function or dominant negative effects (**Figure 2G**). The common variant R282H showed a small shift in ΔΔG, consistent with it being presumed benign. We also analyzed the evolutionary conservation of the specific amino acids altered in patients with neurodevelopmental defects. All amino acid locations show conservation throughout vertebrate and invertebrate animals; remarkably, V88 and K184 are also conserved in the yeast ortholog, Hfl1 (**Figure 2H**). Overall, this analysis provides insight into the potential disruptive effects of the identified patient variants.

The Zebrafish Ortholog of *TMEM184B* is Involved in Zebrafish Development

medRxiv preprint doi: https://doi.org/10.1101/2024.06.27.24309417; this version posted July 1, 2024. The copyright holder for this preprint (which was not certified by peer review) is the author/funder, who has granted medRxiv a license to display the preprint in perpetuity. It is made available under a CC-BY 4.0 International license .

We and others have shown previously that zebrafish are a robust vertebrate developmental model that can inform not only physiological relevance to neurodevelopmental disease, but also variant effect. To test these possibilities, first we identified the zebrafish TMEM184B ortholog using reciprocal BLAST searches between the human TMEM184B protein, GenBank ID: NP_001182000.1, and the translated zebrafish genome. This query identified two zebrafish orthologs: *tmem184ba,* ENSDARG00000045147; 82% similarity, 80% identity and *tmem184bb*, ENSDARG00000090876; 77% similarity, 74% identity, versus human protein, respectively. Next, we used database and literature searches to find that expression of *tmem184ba* is markedly higher in whole larvae during the first five days of development than *tmem184bb* [24], and that *tmem184ba* has a ~23-fold higher expression level in the zebrafish head at 3 dpf than its paralog.[25] Thus, we reasoned that *tmem184ba* is the most relevant ortholog of *TMEM184B,* and that its spatiotemporal expression in the zebrafish head supported a potential physiological role in neurodevelopment.

To bolster a possible role for *tmem184ba* in formation and function of neural structures, we transiently suppressed its expression with a morpholino (MO) targeting the exon 6 splice donor site (**Supplementary File 3A**). Monitoring of mRNA splicing events in MO-injected larvae with RT-PCR and sequencing of cloned PCR products showed exon 6 exclusion, which removed 92 bp and resulted in a putative premature termination (**Supplementary File 3B, C**). Next, we showed that injection of increasing doses of MO (1 ng, 2 ng, and 3 ng) into WT embryos resulted in a dose-dependent reduction in head size and body length in larvae subjected to automated live bright field imaging at 3 dpf, with the highest dose producing a ~10% reduction in head area (**Supplementary File 3D, E, F**), supporting a role for *TMEM184B* in overall animal growth.

TMEM184B **is Involved in Neurodevelopment and** ***De Novo*** **Missense Variants Confer Dominant Toxic or Loss of Function Effects**

medRxiv preprint doi: https://doi.org/10.1101/2024.06.27.24309417; this version posted July 1, 2024. The copyright holder for this preprint (which was not certified by peer review) is the author/funder, who has granted medRxiv a license to display the preprint in perpetuity. It is made available under a CC-BY 4.0 International license .

Given that all variants in our cohort are heterozygous *de novo* changes, we hypothesized possible molecular mechanisms of dominant toxicity or haploinsufficiency. We and others have shown previously that ectopic expression of human mRNA in zebrafish larvae followed by quantitative phenotyping can inform dominant effects such as dominant negative (variant interacts with WT to produce a phenotype)[26] or dominant toxic (variant gains a new function that is deleterious independent of endogenous WT).[27–29] We used an established paradigm [22] to test for dominant effects by injecting a fixed dose (200 pg) of human *TMEM184B* WT and variant mRNA (V88M, L127R, G162R, K184E and G288A) in WT zebrafish embryos at the one to four cell stage and quantified the head and body size at 3 dpf as proxies for neurodevelopmental and growth deficits of affected humans. In replicate experiments, WT mRNA did not result in any detectable phenotypes compared to controls, but we observed a significant reduction in head size with concomitant reduction in body length for G162R and K184E larvae injected with an equivalent mRNA dose suggesting a dominant effect (**Figure 3A, B, C**). By contrast, overexpression of V88M, L127R, G288A, or R282H, the presumed benign variant, did not result in any detectable alteration of anterior structures or overall animal size (**Figure 3D, E**). Together, these data indicated divergent variant effects.

To dissect further the possibility of dominant negative or dominant toxic (WT dependent versus independent variant effect, respectively), we co-injected embryos with progressively decreasing WT mRNA doses with progressively increasing variant mRNA doses while maintaining the overall human transcript amount constant (200 pg). Using the same phenotyping measures at 3 dpf, we found that for both G162R and K184E all three conditions injected with WT plus variant mRNA resulted in altered head size phenotypes but their effect was not significantly different from 200 pg WT mRNA, indicative of a dominant toxic effect (**Figure 4 A and C**). For body length measurements, we observed significant differences for WT-variant mRNA combinations versus 200 pg variant mRNA alone, but there was no consistent dose-dependent effect that could indicate a dominant negative effect (**Figure 4 B**

medRxiv preprint doi: https://doi.org/10.1101/2024.06.27.24309417; this version posted July 1, 2024. The copyright holder for this preprint (which was not certified by peer review) is the author/funder, who has granted medRxiv a license to display the preprint in perpetuity. It is made available under a CC-BY 4.0 International license .

and D). Although our *in vivo* data could not resolve the precise molecular mechanism of variant action, they suggested that G162R and K184E likely confer pathogenic effects through WT-independent biochemical mechanisms.

Next, we pursued a loss of function hypothesis for V88M, L127R, and G288A by employing a complementation strategy, which compares rescue ability of human WT versus variant *TMEM184B* mRNA in the presence of MO.[22] First, we established experimental parameters in which co-injection of WT mRNA restored larval head and body length phenotypes to measurements indistinguishable from controls (**Figure 5A, B, C**). Next, we compared the rescue of each variant mRNA to either MO alone or WT mRNA; we observed that each of V88M, L127R and G288A rescue both head size and body length phenotypes significantly worse than the WT or the negative control variant, R282H (**Figure 5A, B, C**). These data indicate that these three disease-associated variants confer reduced protein function consistent with a haploinsufficiency basis for disease.

To achieve further resolution into the neuroanatomical phenotypes induced by *tmem184ba* impairment, we performed whole mount staining of 3 dpf zebrafish larvae with acetylated tubulin to demarcate optic tecta and intertectal neurons, established proxies for microcephaly and corpus callosum defects in humans.[30,31] In biological triplicate experiments, we observed a significant reduction in optic tecta size for morphants compared to controls, a phenotype that could be rescued significantly by co-injection of WT human mRNA (**Figure 5D, E**). Additionally, we counted the number of neuronal axon tracts crossing the dorsal midline and found a significant reduction in morphants, which could also be rescued by co-injection of WT human *TMEM184B* (**Fig 5D, F**). These data show discrete neuroanatomical features impaired by *tmem184ba* depletion beyond overall head and animal body growth, and further demonstrate reagent specificity with rescue of MO-induced phenotypes with WT human mRNA.

TMEM184B Variants Affect Protein Expression Levels and Cell Viability

medRxiv preprint doi: https://doi.org/10.1101/2024.06.27.24309417; this version posted July 1, 2024. The copyright holder for this preprint (which was not certified by peer review) is the author/funder, who has granted medRxiv a license to display the preprint in perpetuity. It is made available under a CC-BY 4.0 International license .

To analyze further the cellular consequences of disease-linked *TMEM184B* variants, we modeled their effects by over-expression in a human cell line (HEK293T). Using this model, we hypothesized that dominant effects of patient variants would be detectable. We created mi670-tagged expression constructs of human TMEM184B, containing either the WT form or a variant matching one of the six disease-associated variants. To determine how to model patient 5 (splice acceptor change), we used RT-PCR to amplify and then sequence the area surrounding the variant in induced pluripotent stem cells derived from this affected individual. We identified two primary amplicons, one of which was found to be the canonical sequence. The smaller amplicon showed a complete deletion of exon 7 (**Supplementary File 4**). While other minor species may not have been detected by this analysis, our data suggest that exon 7 deletion (Ex7del) is the primary effect of the IVS8+1G>A variant. Therefore, one of our expression constructs was built to model this deletion. The protein product of an exon 7 deletion is a nonsense variant that removes transmembrane helices 5-6 and terminates the protein shortly thereafter.

Microcephaly could be caused by reduced proliferation of neural progenitors, or by reduced viability of variant-expressing cells in the brain.[32,33] To examine viability of cells expressing patient variants of TMEM184B, we analyzed apoptosis in human cells transiently transfected with each of the six TMEM184B variants. Given the differences in structural stability between variants, we first compared the expression levels of fluorescently tagged versions of all variants to the WT protein expression. This analysis showed that, with one exception (G162R), all patient variant proteins show reduced overall levels compared to WT (**Figure 6A-C and Supplemental File 5**). We have not determined if this is due to nonsense mediated decay of mRNA or to increased degradation of a structurally compromised protein. However, in either case, our data predict that variant proteins are not present in cells at the same level as the WT protein.

medRxiv preprint doi: https://doi.org/10.1101/2024.06.27.24309417; this version posted July 1, 2024. The copyright holder for this preprint (which was not certified by peer review) is the author/funder, who has granted medRxiv a license to display the preprint in perpetuity. It is made available under a CC-BY 4.0 International license .

We then analyzed apoptosis using a flow cytometry assay based on accumulation of Zombie Violet, an amine-reactive dye, in dead cells. In normal media, cells overexpressing K184E, Ex7del, and G288A showed increases in cell death of 2-7x compared to cells overexpressing the WT TMEM184B protein (**Figure 6D-E and Supplemental File 6**). For K184E and Ex7del, this increase in cell death continued after starvation (**Supplementary Figure 5K**).

Variant Expression Disrupts Shuttling of the Lysosomal Biogenesis Transcription Factor EB (TFEB)

Signaling pathways that operate downstream of TMEM184B are unknown, but prior work suggests an intersection between these pathways and the processes of synaptic growth, proliferation, and autophagy.[1,2,7] In cells starved of nutrients, transcription factor EB (TFEB) is dephosphorylated and enters the nucleus to transcribe lysosomal and autophagosomal genes to promote recovery from metabolic stress.[16] Knockdown of *TMEM184B* expression in cell lines alters its starvation-induced distribution, causing prolonged nuclear retention TFEB.[34] We therefore postulated that patient variants might also alter the nuclear-to-cytoplasmic distribution of TFEB. We generated HEK293T cell lines stably expressing TFEB-GFP and H2B-mRuby (nuclear marker), and analyzed the Nuclear:Cytoplasmic ratio of TFEB-GFP in the presence of each TMEM184B patient variant. Strikingly, we found that in normal (unstarved) conditions there were already significant differences in TFEB distribution in the presence of many TMEM184B variants. The variants split into two groups: K184E, Ex7del, and G288A increased the nuclear:cytoplasmic ratio of TFEB, while V88M decreased the ratio (**Figure 7**). TFEB localization varied across all patient variants for six hours, with all of them displaying significant differences in at least one time point (**Figure 7M-N, Supplemental File 7**).

medRxiv preprint doi: https://doi.org/10.1101/2024.06.27.24309417; this version posted July 1, 2024. The copyright holder for this preprint (which was not certified by peer review) is the author/funder, who has granted medRxiv a license to display the preprint in perpetuity. It is made available under a CC-BY 4.0 International license .

To identify concordance between our zebrafish and cellular findings with patient phenotypes, we provide a table aligning clinical features and important discoveries from our models (**Table 2**).

DISCUSSION

Here we present the consequences of *TMEM184B* rare pathogenic variants on human neural development and signaling. While each patient's syndrome has some unique aspects, all six variants we characterized share clinical features including developmental delay or intellectual disability, structural brain disruptions (hypoplastic corpus callosum and/or microcephaly), and/or seizures, indicating that nervous system disruption is a central result of altered TMEM184B function. Interestingly, while our manuscript was in preparation, we learned of an additional patient with a disruption whose syndrome includes all three features noted above (CR, personal communication). In addition to these central nervous system effects, two patients also report gastrointestinal motility disruption, which we suspect could result from enteric innervation pathology. We anticipate that as more *TMEM184B* disorder-linked variants are reported, they will produce scalar modifications to these core nervous system phenotypes.

Our data show that currently known TMEM184B variants cluster into two functional categories. Variants G162R and K184E appear to work in dominant effects, given their ability to induce microcephaly when over-expressed in zebrafish larvae. Dominant toxic classification for these variants is also supported by cellular results showing that K184E or G162R over-expression in HEK293T cells causes increased TFEB nuclear localization following starvation (with K184E causing this change even before starvation). In contrast, variants V88M, L127R, and G288A appear to compromise TMEM184B function and thus produce haploinsufficiency. These variants stratify somewhat in that V88M and L127R cause reduction of TFEB in the nucleus (either before or 1 hour after starvation), whereas

medRxiv preprint doi: https://doi.org/10.1101/2024.06.27.24309417; this version posted July 1, 2024. The copyright holder for this preprint (which was not certified by peer review) is the author/funder, who has granted medRxiv a license to display the preprint in perpetuity. It is made available under a CC-BY 4.0 International license .

G288A causes increased TFEB nuclear localization when overexpressed. The final variant (IVS8+1 G>A) is predicted to cause a frameshift and predicted truncation in the TMEM184B protein due to the deletion of exon 7. Other minor mRNA species may also be produced (for example, by splicing to a cryptic acceptor found in the intron just after the variant). Our attempts to model exon 7 deletion in cells indicate that this variant has reduced protein quantity compared to WT and triggers substantial apoptosis of variant-expressing cells. Further work is needed to fully define the spectrum of isoforms produced by this splice alteration and their effects on function.

Overall, our data align with prior work showing the effects of significant loss of function of TMEM184B in both *Drosophila* and mice. While the overall size of the brain was not examined, mice with a genetic disruption of *TMEM184B* (95% reduction in transcript levels) show abnormally swollen intraepidermal nerve fibers (endings of sensory neurons) and swollen motor neuron presynaptic terminals at neuromuscular junctions.[1] Similarly in flies, mutation of the *TMEM184B* ortholog *tmep* causes abnormal presynaptic sprouting.[2] This may suggest that, in variants that confer a dominant effect such as K184E, synaptic structure may be compromised. Future work should examine variant effect on synapses *in vivo* using knock-in models of heterozygous variant expression, matching the genotype and zygosity of affected individuals.

While initial studies in rodent and fly models suggested a link to neurodegenerative diseases like ALS, our cohort highlights that the nervous system disruptions caused by *TMEM184B* alteration happen much earlier. TMEM184B-associated syndromes resemble other juvenile-onset disorders of abnormal metabolism including the lysosomal storage disorder Niemann-Pick Type C (NPC) caused by pathogenic variation in one of two lipid transporters (NPC1 or NPC2). Cellular phenotypes of NPC include accumulated lipids in the endolysosomal system, similar to what is seen in mouse models of TMEM184B loss-of-function.[35–37] In mice containing a disease-associated NPC1 mutation (D1005G)[38],

medRxiv preprint doi: https://doi.org/10.1101/2024.06.27.24309417; this version posted July 1, 2024. The copyright holder for this preprint (which was not certified by peer review) is the author/funder, who has granted medRxiv a license to display the preprint in perpetuity. It is made available under a CC-BY 4.0 International license .

TFEB is erroneously enriched in the nucleus, similar to what we find in the presence of some TMEM184B patient variants. These commonalities suggest that the pathways leading to NPC and TMEM184B-associated disorders share some downstream effects. Numerous other rare disorders cause aberrant TFEB nuclear translation, including Mucolipidosis type IV (MLIV). Another similar disorder with corpus callosum hypoplasia, intellectual disability, and seizures is caused by loss of MYCBP2 (also called PHR1 (mice), Highwire (*Drosophila*) or Rpm-1 (*C. elegans*)), a RING finger ubiquitin ligase known for roles in synapse development.[39–41] TMEM184B and MYCBP2/Phr1/Highwire mutants both show excessively branched synapses and delays in injury-induced axonal degeneration, though the effect of TMEM184B loss is more subtle.[42,43,1,2] It will be of interest to explore the intersections of these proteins in the context of neural development as well as axon degeneration.

In human cells expressing the K184E variant of TMEM184B, the dramatic increase in TFEB nuclear localization may be a compensatory response to nutrient deprivation or disrupted autophagosomal or endolysosomal flux (here used to describe the fusion and maturation of these degradative compartments, both of which end up depositing contents into lysosomes). The K184E variant expressing cells are also more likely to undergo apoptosis, even under nutrient rich conditions. These results could indicate that TMEM184B participates in autophagic or endolysosomal flux, ensuring lysosomal cargo degradation and promoting cellular survival. Patient variants like K184E that severely disrupt TMEM184B stability and function would therefore cause excessive cell death during development and could directly lead to microcephaly or other severe disease presentation. Variants that more subtly alter flux in the cell (indicated by abnormally high or low nuclear-to-cytoplasmic ratio) could impair axon outgrowth pathways necessary to establish the cross-hemispheric connections of the corpus callosum.

medRxiv preprint doi: https://doi.org/10.1101/2024.06.27.24309417; this version posted July 1, 2024. The copyright holder for this preprint (which was not certified by peer review) is the author/funder, who has granted medRxiv a license to display the preprint in perpetuity. It is made available under a CC-BY 4.0 International license .

Our structural modeling of each of the known patient variants indicates substantial alterations in the alignment of alpha-helices, and consequent changes in overall protein stability. Here also we find two categories of changes: three variants (K184E, G162R, and V88M) overly stabilize the TMEM184B protein (indicated by negative values < -10), while two variants (L127R and G288A) destabilize the protein (positive values > 10). With one exception (V88M), these structural predictions align with the classifications of variants as causing dominant effects (K184E and G162R) or haploinsufficiency (L127R and G288A). TMEM184B is annotated as a putative transporter,[44–46] though the transported substance is as yet unknown. If we consider this possible function in our working model, over-stability of a transporter would likely be quite deleterious, as it could be locked into a conformation that would prevent the flexibility needed to facilitate movement of its transport substrate. Given the dominant effects of K184E and G162R, it is possible that these form dimers with WT TMEM184B protein and could prevent its transporter function or other function in the cell. It is also possible that K184 and G162R could work another way, for example by creating "leaky" transporters that equilibrate their substrate across endosomal membranes. Gradients of ions (like H+) set the proper pH inside endosomal and lysosomal compartments, which is important for proper fusion, flux, and degradation of contents.[47] If these gradients were disrupted, autophagosomes and lysosomes would not be able to effectively degrade their contents, a result matching what is seen when TMEM184B is disrupted in mice.[1]

We observe that for all affected individuals with corpus callosum hypoplasia, their respective variants cause an *increased* TFEB nuclear localization at one or more points in our time course (4/4), while variants of patients not diagnosed with corpus callosum hypoplasia (but with other neurodevelopmental defects) show a *decreased* TFEB nuclear localization at one or more time points. While this alignment in TFEB alteration and diagnosis could change as new patients are discovered, it may also be an indicator that

medRxiv preprint doi: https://doi.org/10.1101/2024.06.27.24309417; this version posted July 1, 2024. The copyright holder for this preprint (which was not certified by peer review) is the author/funder, who has granted medRxiv a license to display the preprint in perpetuity. It is made available under a CC-BY 4.0 International license .

variants which cause cells to act as if they are nutrient depleted would suppress developmental processes that are highly energy-intensive, such as axon outgrowth. Notably, a recent RNAseq analysis of embryonic neurons from TMEM184B mutant mice showed that the most significantly altered biological process is axonogenesis, followed closely by axon development and neuron differentiation.[4]

Our study demonstrates the connection between TMEM184B sequence variation and human neurodevelopmental disease and provides mechanistic information about how variants dominantly disrupt protein structure and metabolic signaling. However, many details remain unknown. For one, our predictions of the molecular function of TMEM184B are based solely on sequence and structural homology. These studies suggest that TMEM184B and its related family members (TMEM184A and TMEM184C) belong in a large and diverse family including transporters, opsins, and G-protein coupled receptors.[46] We also need to better understand how TMEM184B activity and TFEB signaling are connected. TFEB nuclear translocation is inhibited by phosphorylation, which can occur through at least four different kinase pathways: mTORC1, ERK2, Akt, and GSK3b.[48] Determining which of these pathways are disrupted by mutation or deletion of TMEM184B, and precisely how TMEM184B influences these well-established growth control pathways directly or indirectly, is a high priority for future study.

A caveat in our modeling of TMEM184B associated disorders is that none of these models perfectly reproduce the human inheritance pattern. All patients show heterozygous expression of a variant form alongside a normal protein. While the dominant effects of the variants studied here permitted us to investigate their effects via transient expression in WT backgrounds, the overall dosage of TMEM184B protein is higher than normal in these scenarios. Future work should use gene or base editing to introduce patient variants in a heterozygous background using model organisms or cell lines, where dosage of the two

medRxiv preprint doi: https://doi.org/10.1101/2024.06.27.24309417; this version posted July 1, 2024. The copyright holder for this preprint (which was not certified by peer review) is the author/funder, who has granted medRxiv a license to display the preprint in perpetuity. It is made available under a CC-BY 4.0 International license .

forms of the protein matches affected humans. In these models, we can better examine neuronal differentiation and axon guidance under physiologically relevant conditions.

Research Contributions

M.R.C.B., E.E.D., S.B. and K.A.C. initiated the project. K.A.C. coordinated the organization of clinical information from the patient cohort. F.U. performed all zebrafish modeling experiments and data analysis. Z.Y. performed all human cell experiments and data analysis. S.V.K. and S.S. performed structural modeling and analysis. S.P.C, T.S., C.S., N.M., H.F., E.T., J.T.-S., A.A., V.S., P.S., and S.C. contributed clinical data for the patients. K.P. helped create reporter cell lines and assisted with data analysis. Z.Y., F.U., K.C., S.S., E.E.D., and M.R.C.B. wrote the paper.

Acknowledgments

We thank Dr. Curtis Thorne for access to his widefield microscope, staff of the University of Arizona Flow Cytometry Shared Resource, and staff of the Nikon Imaging Center of Excellence at the University of Arizona for their support. Funding for this work was provided by NIH R01 NS105680 (M.R.C.B.), NIH R01 MH106826 (E.E.D.) and a Core Facility Pilot Award from the University of Arizona (M.R.C.B.). We would also like to thank all the subjects and their families for participating in this research. E.E.D. is the Ann Marie and Francis Klocke, M.D. Research Scholar.

REFERENCES

1. Bhattacharya, M. R. C. *et al.* TMEM184b Promotes Axon Degeneration and Neuromuscular Junction Maintenance. *J. Neurosci.* **36**, 4681–9 (2016).
2. Cho, T. S., Beigaitė, E., Klein, N. E., Sweeney, S. T. & Bhattacharya, M. R. C. The Putative Drosophila TMEM184B Ortholog Tmep Ensures Proper Locomotion by Restraining Ectopic

medRxiv preprint doi: https://doi.org/10.1101/2024.06.27.24309417; this version posted July 1, 2024. The copyright holder for this preprint (which was not certified by peer review) is the author/funder, who has granted medRxiv a license to display the preprint in perpetuity. It is made available under a CC-BY 4.0 International license .

Firing at the Neuromuscular Junction. *Mol. Neurobiol.* (2022) doi:10.1007/S12035-022-02760-3.

3. Wright, E. B., Larsen, E. G., Coloma-Roessle, C. M., Hart, H. R. & Bhattacharya, M. R. C. Transmembrane protein 184B (TMEM184B) promotes expression of synaptic gene networks in the mouse hippocampus. *BMC Genomics* **24**, 559 (2023).
4. Larsen, E. G. *et al.* Transmembrane protein TMEM184B is necessary for interleukin-31-induced itch. *Pain* **163**, E642–E653 (2022).
5. Oliva, C. A., Montecinos-Oliva, C. & Inestrosa, N. C. Chapter Three - Wnt Signaling in the Central Nervous System: New Insights in Health and Disease. in *Progress in Molecular Biology and Translational Science* (eds. Larraín, J. & Olivares, G.) vol. 153 81–130 (Academic Press, 2018).
6. Yao, Z. *et al.* A high-resolution transcriptomic and spatial atlas of cell types in the whole mouse brain. *Nature* **624**, 317–332 (2023).
7. Lin, Y., Liu, D., Li, X., Ma, Y. & Pan, X. TMEM184B promotes proliferation, migration and invasion, and inhibits apoptosis in hypopharyngeal squamous cell carcinoma. *J. Cell. Mol. Med.* **26**, 5551–5561 (2022).
8. Fukumoto, I. *et al.* MicroRNA expression signature of oral squamous cell carcinoma: functional role of microRNA-26a/b in the modulation of novel cancer pathways. *Br. J. Cancer* **112**, 891–900 (2015).
9. Lindström, S. *et al.* Genome-wide association study identifies multiple loci associated with both mammographic density and breast cancer risk. *Nat. Commun.* **5**, 5303 (2014).
10. Baxter, S. M. *et al.* Centers for Mendelian Genomics: A decade of facilitating gene discovery. *Genet. Med.* **24**, 784–797 (2022).
11. Hüppi, P. S. *et al.* Quantitative magnetic resonance imaging of brain development in premature and mature newborns. *Ann. Neurol.* **43**, 224–235 (1998).
12. Takahashi, E., Folkerth, R. D., Galaburda, A. M. & Grant, P. E. Emerging Cerebral

medRxiv preprint doi: https://doi.org/10.1101/2024.06.27.24309417; this version posted July 1, 2024. The copyright holder for this preprint (which was not certified by peer review) is the author/funder, who has granted medRxiv a license to display the preprint in perpetuity. It is made available under a CC-BY 4.0 International license .

Connectivity in the Human Fetal Brain: An MR Tractography Study. *Cereb. Cortex* **22**, 455–464 (2012).

13. Dawidziuk, M. *et al.* Exome Sequencing Reveals Novel Variants and Expands the Genetic Landscape for Congenital Microcephaly. *Genes* **12**, 2014 (2021).
14. Hsu, C. L. *et al.* MAP4K3 mediates amino acid-dependent regulation of autophagy via phosphorylation of TFEB. *Nat. Commun.* **9**, 942 (2018).
15. Martina, J. A., Chen, Y., Gucek, M. & Puertollano, R. MTORC1 functions as a transcriptional regulator of autophagy by preventing nuclear transport of TFEB. *Autophagy* **8**, 903–914 (2012).
16. Sardiello, M. *et al.* A gene network regulating lysosomal biogenesis and function. *Science* **325**, 473–477 (2009).
17. Napolitano, G. & Ballabio, A. TFEB at a glance. *J. Cell Sci.* **129**, 2475–2481 (2016).
18. Cunningham, K. M. *et al.* TFEB/Mitf links impaired nuclear import to autophagolysosomal dysfunction in C9-ALS. *eLife* **9**, e59419 (2020).
19. Sobreira, N., Schiettecatte, F., Valle, D. & Hamosh, A. GeneMatcher: a matching tool for connecting investigators with an interest in the same gene. *Hum. Mutat.* **36**, 928–930 (2015).
20. Cheng, J. *et al.* Accurate proteome-wide missense variant effect prediction with AlphaMissense. *Science* **381**, eadg7492 (2023).
21. Ruff, K. M. & Pappu, R. V. AlphaFold and Implications for Intrinsically Disordered Proteins. *J. Mol. Biol.* **433**, 167208 (2021).
22. Niederriter, A. R. *et al.* In Vivo Modeling of the Morbid Human Genome using Danio rerio. *J. Vis. Exp. JoVE* (2013) doi:10.3791/50338.
23. Isrie, M. *et al.* Mutations in Either TUBB or MAPRE2 Cause Circumferential Skin Creases Kunze Type. *Am. J. Hum. Genet.* **97**, 790 (2015).
24. White, R. J. *et al.* A high-resolution mRNA expression time course of embryonic development in zebrafish. *eLife* **6**, e30860 (2017).

medRxiv preprint doi: https://doi.org/10.1101/2024.06.27.24309417; this version posted July 1, 2024. The copyright holder for this preprint (which was not certified by peer review) is the author/funder, who has granted medRxiv a license to display the preprint in perpetuity. It is made available under a CC-BY 4.0 International license .

25. Lee, Y.-R. *et al.* Mutations in FAM50A suggest that Armfield XLID syndrome is a spliceosomopathy. *Nat. Commun.* **11**, (2020).

26. Sarparanta, J. *et al.* Mutations affecting the cytoplasmic functions of the co-chaperone DNAJB6 cause limb-girdle muscular dystrophy. *Nat. Genet.* **44**, 450–455 (2012).

27. Guissart, C. *et al.* Dual Molecular Effects of Dominant RORA Mutations Cause Two Variants of Syndromic Intellectual Disability with Either Autism or Cerebellar Ataxia. *Am. J. Hum. Genet.* **102**, 744–759 (2018).

28. Gordon, C. T. *et al.* Mutations in the Endothelin Receptor Type A Cause Mandibulofacial Dysostosis with Alopecia. *Am. J. Hum. Genet.* **96**, 519–531 (2015).

29. Tan, P. L. *et al.* Systematic Functional Testing of Rare Variants: Contributions of CFI to Age-Related Macular Degeneration. *Invest. Ophthalmol. Vis. Sci.* **58**, 1570–1576 (2017).

30. Grange, L. J. *et al.* Pathogenic variants in SLF2 and SMC5 cause segmented chromosomes and mosaic variegated hyperploidy. *Nat. Commun.* **13**, 6664 (2022).

31. Ansar, M. *et al.* Bi-allelic Variants in DYNC1I2 Cause Syndromic Microcephaly with Intellectual Disability, Cerebral Malformations, and Dysmorphic Facial Features. *Am. J. Hum. Genet.* **104**, 1073–1087 (2019).

32. Gilmore, E. C. & Walsh, C. A. Genetic causes of microcephaly and lessons for neuronal development. *Wiley Interdiscip. Rev. Dev. Biol.* **2**, 461–478 (2013).

33. Jayaraman, D., Bae, B.-I. & Walsh, C. A. The Genetics of Primary Microcephaly. *Annu. Rev. Genomics Hum. Genet.* **19**, 177–200 (2018).

34. Kanfer, G. *et al.* Image-based pooled whole-genome CRISPRi screening for subcellular phenotypes. *J. Cell Biol.* **220**, (2021).

35. Liscum, L., Ruggiero, R. M. & Faust, J. R. The intracellular transport of low density lipoprotein-derived cholesterol is defective in Niemann-Pick type C fibroblasts. *J. Cell Biol.* **108**, 1625–1636 (1989).

36. Lloyd-Evans, E. *et al.* Niemann-Pick disease type C1 is a sphingosine storage disease

medRxiv preprint doi: https://doi.org/10.1101/2024.06.27.24309417; this version posted July 1, 2024. The copyright holder for this preprint (which was not certified by peer review) is the author/funder, who has granted medRxiv a license to display the preprint in perpetuity. It is made available under a CC-BY 4.0 International license .

that causes deregulation of lysosomal calcium. *Nat. Med.* **14**, 1247–1255 (2008).

37. Maue, R. A. *et al.* A novel mouse model of Niemann-Pick type C disease carrying a D1005G-Npc1 mutation comparable to commonly observed human mutations. *Hum. Mol. Genet.* **21**, 730–750 (2012).

38. Kim, S. *et al.* Disruptive lysosomal-metabolic signaling and neurodevelopmental deficits that precede Purkinje cell loss in a mouse model of Niemann-Pick Type-C disease. *Sci. Rep.* **13**, 5665 (2023).

39. Wan, H. I. *et al.* Highwire regulates synaptic growth in Drosophila. *Neuron* **26**, 313–329 (2000).

40. Collins, C. A., Wairkar, Y. P., Johnson, S. L. & DiAntonio, A. Highwire Restrains Synaptic Growth by Attenuating a MAP Kinase Signal. *Neuron* **51**, 57–69 (2006).

41. AlAbdi, L. *et al.* Loss-of-function variants in MYCBP2 cause neurobehavioural phenotypes and corpus callosum defects. *Brain J. Neurol.* **146**, 1373–1387 (2023).

42. Xiong, X. *et al.* The Highwire ubiquitin ligase promotes axonal degeneration by tuning levels of Nmnat protein. *PLoS Biol.* **10**, e1001440 (2012).

43. Babetto, E., Beirowski, B., Russler, E. V., Milbrandt, J. & DiAntonio, A. The Phr1 ubiquitin ligase promotes injury-induced axon self-destruction. *Cell Rep.* **3**, 1422–1429 (2013).

44. Dawson, P. A. *et al.* The heteromeric organic solute transporter alpha-beta, Ostalpha-Ostbeta, is an ileal basolateral bile acid transporter. *J. Biol. Chem.* **280**, 6960–6968 (2005).

45. Malinovsky, F. G. *et al.* Lazarus1, a DUF300 Protein, Contributes to Programmed Cell Death Associated with Arabidopsis acd11 and the Hypersensitive Response. *PLoS ONE* **5**, e12586 (2010).

46. Yee, D. C. *et al.* The transporter-opsin-G protein-coupled receptor (TOG) superfamily. *FEBS J.* **280**, 5780–800 (2013).

47. Mauthe, M. *et al.* Chloroquine inhibits autophagic flux by decreasing

medRxiv preprint doi: https://doi.org/10.1101/2024.06.27.24309417; this version posted July 1, 2024. The copyright holder for this preprint **(which was not certified by peer review)** is the author/funder, who has granted medRxiv a license to display the preprint in perpetuity. It is made available under a CC-BY 4.0 International license .

autophagosome-lysosome fusion. *Autophagy* **14**, 1435–1455 (2018).

48. Palmieri, M. *et al.* mTORC1-independent TFEB activation via Akt inhibition promotes cellular clearance in neurodegenerative storage diseases. *Nat. Commun.* **8**, 14338 (2017).

medRxiv preprint doi: https://doi.org/10.1101/2024.06.27.24309417; this version posted July 1, 2024. The copyright holder for this preprint (which was not certified by peer review) is the author/funder, who has granted medRxiv a license to display the preprint in perpetuity. It is made available under a CC-BY 4.0 International license .

Figure Legends

Table 1. Patients in the current study contain rare sequence variants within the *TMEM184B* locus.

All affected individuals whose variants were modeled in this study are shown. Allele frequency was determined by search of the gnomAD database (v4.1.0). AlphaMissense scores predict the likelihood of a missense variant to be pathogenic (highest likelihood = 1, lowest likelihood = 0). Patient 5 could not be calculated because the sequence change results in a splice acceptor mutation, not a missense variant. Abbreviations: CC, corpus callosum; m, months; y, years; F, female; M, male; N/A, not applicable; ND, not done.

Figure 1: Brain magnetic resonance imaging (MRI) shows corpus callosum hypoplasia in two patients with *TMEM184B* variants.

A Sagittal plane of spoiled gradient recalled acquisition (SPGR) MRI in a patient of the same age as patient 5 who has an unrelated gene variant and shows no alterations in corpus callosum thickness. **B** Sagittal T2 MRI in patient 4 (K184E) shows corpus callosum disruption. **C** Sagittal SPGR MRI in patient 5 (c.589+1 G>A) shows corpus callosum hypoplasia.

Supplemental File 1. **Survey for Patient Data Collection**

This file includes the patient data collection survey used for providers to compile diagnostic and clinical information.

Supplemental File 2. Detailed Clinical Data on Affected Individuals

medRxiv preprint doi: https://doi.org/10.1101/2024.06.27.24309417; this version posted July 1, 2024. The copyright holder for this preprint (which was not certified by peer review) is the author/funder, who has granted medRxiv a license to display the preprint in perpetuity. It is made available under a CC-BY 4.0 International license .

This file includes details of clinical diagnosis, other genetic changes seen during sequencing, and complete symptom information.

Figure 2. Structural modeling and free energy of TMEM184B variants indicates significant disruptions to protein stability.

A Structure of the human *TMEM184B* transcript (NM_001195071.1). Blue and gray blocks show alternating exons of the spliced mRNA. Red arrow indicates the coding region of isoform a (NP_001182000.1). Areas predicted to be included in transmembrane helices (green) and locations of human variants (black) are noted. **B** Ramachandran plot showing that the structure predicted by FoldX analysis shows only allowable angles, providing confidence in the structure predicted. **C** Predicted local-distance difference test (pLDDT) scores per position across the whole protein sequence. Higher scores indicate higher confidence structural predictions in that region of the protein. **D** Native protein structure prediction by FoldX. Transmembrane helices are separately colorized. **E** V88M variant protein (magenta) overlaid onto the native TMEM184B structure (cyan). **F** K184E variant protein (green) overlaid onto the native TMEM184B structure (cyan). **G** Stability analysis calculations using Gibbs free energy. ΔΔG values that are positive indicate decreased protein stability of variant-containing TMEM184B when compared to the predicted native structure, while negative values indicate abnormally heightened protein structural stability. **H** Amino acid context for the V88M and K184E variants, both of which are conserved from yeast (*Saccaromyces cerevisciae* Hfl1) to humans. All other variants are conserved from *Drosophila* (Tmep) to human but are not found in yeast.

Supplementary File 3. Reagents to transiently suppress *tmem184ba* are efficient.

A Schematic of the zebrafish *tmem184ba* transcript at chr12:19,320,657-19,340,220 (GRCz11). White boxes, untranslated regions; black boxes, coding exons; horizontal black line, introns;

medRxiv preprint doi: https://doi.org/10.1101/2024.06.27.24309417; this version posted July 1, 2024. The copyright holder for this preprint (which was not certified by peer review) is the author/funder, who has granted medRxiv a license to display the preprint in perpetuity. It is made available under a CC-BY 4.0 International license .

vertical arrow, morpholino (MO) target site at the exon 6 splice donor site. **B** Inverted agarose gel image showing RT-PCR products amplified with primers flanking the MO target site in controls and *tmem184ba* morphants. The expected WT band size is 375 bp and morphants have undetectable WT with exon 6 exclusion (92 bp) when injected with 3 ng, 6 ng, or 9 ng MO. **C** Sanger sequence chromatograms confirm exon 6 skipping in morphants injected with 3 ng MO. **D** Representative lateral bright field images of 3 dpf larvae injected with increasing doses of *tmem184ba* MO. Scale bar, 300 µm. **E** Quantification of the lateral head size in 3 dpf larvae as indicated with anatomical landmarks in Figure 1A. Experimental conditions were normalized and presented as a percentage of the control mean. **F** Quantification of the body length in 3 dpf larvae as indicated with anatomical landmarks in Figure 1A. Experimental conditions were normalized and presented as a percentage of the control mean. For panels E and D, statistical analyses were performed with an unpaired student's t-test; ***$p<0.001$; and ns, not significant. n = 40–67/condition. Error bars represent standard deviation of the mean. Data point color: black, uninjected control; red, MO-injected.

Figure 3. Ectopic expression of *TMEM184B* variants G162R or K184E induces head size and body length phenotypes in zebrafish larvae.

A Representative bright field lateral images of 3 day post-fertilization (dpf) larvae injected with 200 pg human *TMEM184B* mRNA (WT, G162R, K184E and R282H). R282H is a presumed benign negative control (dbSNP: rs370107940; 215 heterozygotes and 4 homozygotes are present in 1609748 individuals in gnomAD v4.1.0. Scale bar, 300 µm. Head area was measured according to white dashed line; body length was measured according to the red dashed line. **B and C** Quantification of the lateral head size in 3 dpf larvae. Experimental conditions were normalized and presented as a percentage of the control mean. **D and E** Quantification of the body length in 3 dpf larvae. Experimental conditions were normalized and presented as a percentage of the control mean. Statistical analyses were performed with an unpaired student's

medRxiv preprint doi: https://doi.org/10.1101/2024.06.27.24309417; this version posted July 1, 2024. The copyright holder for this preprint (which was not certified by peer review) is the author/funder, who has granted medRxiv a license to display the preprint in perpetuity. It is made available under a CC-BY 4.0 International license .

t-test; ****p<0.0001; ***p<0.001; and ns, not significant; n = 50–87/condition. Error bars represent standard deviation of the mean. Data point color: black, uninjected control; blue, WT; red, variants identified in affected individuals; green, presumed benign variant from gnomAD.

Figure 4. Titration of G162R or K184E mRNAs with WT *TMEM184B* mRNA to dissect dominant negative or dominant toxic effects.

A and B Quantification of the lateral head size in 3 dpf larvae injected with titrated doses of WT with variant mRNA. Experimental conditions were normalized and presented as a percentage of the control mean. See Figure 1A for anatomical landmarks measured. **C and D** Quantification of the body length in 3 dpf larvae injected with titrated doses of WT with variant mRNA. Experimental conditions were normalized and presented as a percentage of the control mean. See Figure 1A for anatomical landmarks measured. Statistical analyses were performed with an unpaired student's t-test; ****p<0.0001; ***p<0.001; **p<0.01; *p<0.05; and ns, not significant; n = 49–72/condition. Error bars represent standard deviation of the mean. Data point color: black, uninjected control; blue, WT; red, variants identified in affected individuals. Large triangles indicate decreasing or increasing amounts of WT (blue) or variant (red) mRNA.

Figure 5. Loss of *tmem184ba* results in neuroanatomical defects and *in vivo* complementation shows that some disease associated variants result in loss of function.

A Representative bright field lateral images of 3 dpf larvae injected with MO with or without human *TMEM184B* mRNA (WT, V88M, L127R, G288A and R282H). R282H is a presumed benign negative control (dbSNP: rs370107940; 215 heterozygotes and 4 homozygotes are present in 1609748 individuals in gnomAD v4.1.0. Scale bar, 300 μm. Head area was measured according to anatomical landmarks shown in Figure 1A. **B** Quantification of the lateral head size in 3 dpf larvae as indicated with anatomical landmarks in Figure 1A. Experimental conditions were normalized and presented as a percentage of the control mean. **C** Quantification of the

medRxiv preprint doi: https://doi.org/10.1101/2024.06.27.24309417; this version posted July 1, 2024. The copyright holder for this preprint (which was not certified by peer review) is the author/funder, who has granted medRxiv a license to display the preprint in perpetuity. It is made available under a CC-BY 4.0 International license .

body length in 3 dpf larvae as indicated with anatomical landmarks in Figure 1A. Experimental conditions were normalized and presented as a percentage of the control mean. For panels B and C, n = 50–88/condition. **D** Representative dorsal images of 3 dpf larval heads painted with acetylated tubulin. White dotted shape, optic tecta; white dotted line, midline between optic tecta where intertectal commissural axons were counted. Zoomed image at right of each panel corresponds to white box around both optic tecta. Anterior, left; posterior, right; Scale bar, 50 µm. **E** Quantification of optic tecta size as shown in panel D. **F** Quantification of intertectal neurons that cross the dorsal midline as shown in panel E. For panels E and F, n = 30–47/condition. For panels B, C, E and F, statistical analyses were performed with an unpaired student's t-test; ****p<0.0001; ***p<0.001; **p<0.01, *p<0.05, and ns, not significant. Error bars represent standard deviation of the mean. Data point color: black, uninjected control; blue, WT; red, variants identified in affected individuals; green, presumed benign variant from gnomAD.

Supplemental File 4. Evidence for exon 7 deletion in Patient 5.

A RT-PCR and gel electrophoresis from cells from Patient 5 and a control individual. The PCR product spans exons 6-8 and has 941 base pairs. In patient 5 the expected band is accompanied by a smaller band. **B** bands from the above gel were separated, gel purified, Sanger sequenced, and compared to the control. Alignment of the sequences confirms a deletion of exon 7 in the lower band from Patient 5.

Figure 6. TMEM184B variants affect protein expression levels and cell viability

A and B Histogram of miRFP670 fluorescence indicating expression levels of WT vs. (A) K184E or (B) V88M variants. **C** Average fluorescence of TMEM184B variants normalized to WT (N=3 trials). Error bars represent SEM. **D** FACS plots of HEK293T cells over-expressing native TMEM184B (top row) or K184E variant (bottom row) under non-starved or 6 hour-starved

medRxiv preprint doi: https://doi.org/10.1101/2024.06.27.24309417; this version posted July 1, 2024. The copyright holder for this preprint (which was not certified by peer review) is the author/funder, who has granted medRxiv a license to display the preprint in perpetuity. It is made available under a CC-BY 4.0 International license .

conditions. Numbers indicate the percentage of dead cells among non-transfected HEK293T cells (left, calculated by dividing top left cell count by overall untransfected cell count left of the white line) or TMEM184B-transfected HEK293T cells (right, calculated by dividing top right cell count by overall transfected cell count right of the white line). **E** Percentage of dead TMEM184B variant expressing cells normalized to WT (N=3 trials). In panels C and E, error bars represent SEM. ****p<0.0001, **p<0.01.

Supplemental File 5. Raw data showing expression levels of TMEM184B variants.

A-D Expression distributions for (A) L127R, (B) G162R, (C) Ex7del (IVS8+1G>A), and (D) G288A (all in red) compared to WT (blue).

Supplemental File 6. Cell death assay of TMEM184B variants overexpressed in HEK293T cells.

Flow cytometry evaluation of cell viability in HEK293T cells transfected with the indicated TMEM184B patient variants. **A-J** FACS plots of non-starved and six-hour starved cells from (A-B) V88M overexpressing cells, (C-D) L127R overexpressing cells, (E-F) G162R overexpressing cells, (G-H) Ex7del (IVS8+1G>A) overexpressing cells, and (I-J) G288A overexpressing cells. **K** percentage of dead TMEM184B variant expressing cells that were starved for six hours, quantified as in Figure 5 (N=3 trials). Error bars represent SEM. *p<0.05.

Figure 7. TFEB nuclear-to-cytoplasmic ratio is dominantly altered by expression of patient TMEM184B variants.

A-D and G-J Multichannel images of non-starved HEK293T cells overexpressing WT or K184E, respectively. TFEB-GFP (A and G), H2B-mRuby (B and H), TMEM184B-miRFP6670 (C and I), and merge (D and J). **E-F and K-L** are WT and K184E cells starved for one hour, respectively. TFEB-GFP (E and K) and merge (F and L). Arrows in all images point to TMEM184B-miRFP670

medRxiv preprint doi: https://doi.org/10.1101/2024.06.27.24309417; this version posted July 1, 2024. The copyright holder for this preprint (which was not certified by peer review) is the author/funder, who has granted medRxiv a license to display the preprint in perpetuity. It is made available under a CC-BY 4.0 International license .

transfected cells. All H2B-mRuby images had their Lookup Tables adjusted to 4000 for visual clarity. **M** Ratio of mean TFEB-GFP fluorescence in the nucleus vs. cytoplasm in TMEM184B-miRFP670 expressing cells, normalized to non-starved WT cells. **N** Timelapse of TFEB localization (nucleus vs. cytoplasm) of K184E and IVS8+1G>A (exon 7 deletion) expressing cells at baseline, one hour, and six hour starvation timepoints (N=3 trials). M and N error bars represent SEM. ****p<0.0001, *p<0.01. 50 cells were quantified in every trial for every patient variant and time point except for K184E at six hour starvation (42-50 cells) and Ex7del at all time points. At no starvation, one hour, and six hours, we quantified between 43-50, 42-50, and 14-42 cells respectively.

Supplemental File 7. TFEB localization is altered by TMEM184B patient variants.

A and B TFEB localization in HEK293T cells overexpressing TMEM184B patient variants at one-hour and six-hour starvation time points respectively. All conditions were normalized to non-starved WT cells (N=3 trials). **C-H** Ratio of nuclear to cytoplasmic TFEB localization of patient variant expressing cells over six hours compared to WT. C, V88M vs. WT. D, L127R vs. WT. E, G162R vs. WT. F, K184E vs. WT. G, Ex7del (IVS8+1G>A) vs. WT. H, G288A vs. WT. Error bars in A-H represent SEM. Some error bars were unable to be graphed because they were too small in relation to their respective time point. **I** Table summarizing TFEB localization for the six TMEM184B patient variants. Blue asterisks indicate significant decreases in localization compared to WT. Red asterisks indicate significant increases in localization compared to WT. ****p<0.0001, ***p<0.001, **p<0.01, *p<0.05.

Table 2. Summary of clinical, zebrafish model, and TFEB results. Abbreviations: DD, developmental delay; ID, intellectual disability; HCC, hypoplastic corpus callosum; DN, dominant negative; ΔΔG, change in Gibbs free energy between variant and WT; ND, not done; Var, variable; ZF, zebrafish.

Patient	Age of diagnosis	Gender (assigned at birth)	Genotype	Origin	Protein prediction	Method of detection	Allele frequency	alpha-missense score	Developmental delay or Intellectual disability	Micro-cephaly	Thin or hypo-plastic CC	Seizures
1	0-5 y	F	c.262 G>A	De novo	V88M	Whole exome	0.000029%	0.902				
2	unknown	M	c.380 T>G	De novo	L127R	Whole exome	Not in Gnomad	0.981				
3	0-5 y	F	c.484 G>A	De novo	G162R	Whole exome	Not in Gnomad	0.697				
4	0-5 y	M	c.550 A>G	De novo	K184E	Whole genome	Not in Gnomad	0.984				
5	6-10 y	F	c.787+1G>A	De novo	IVS8+1G>A	Whole exome	Not in Gnomad	N/A				
6	6-10 y	M	c.863 G>C	De novo	G288A	Whole exome	Not in Gnomad	0.628				

Detailed clinical information has been removed in accordance with medRxiv policies. Please contact the corresponding authors to request access to these data.

Figure 1

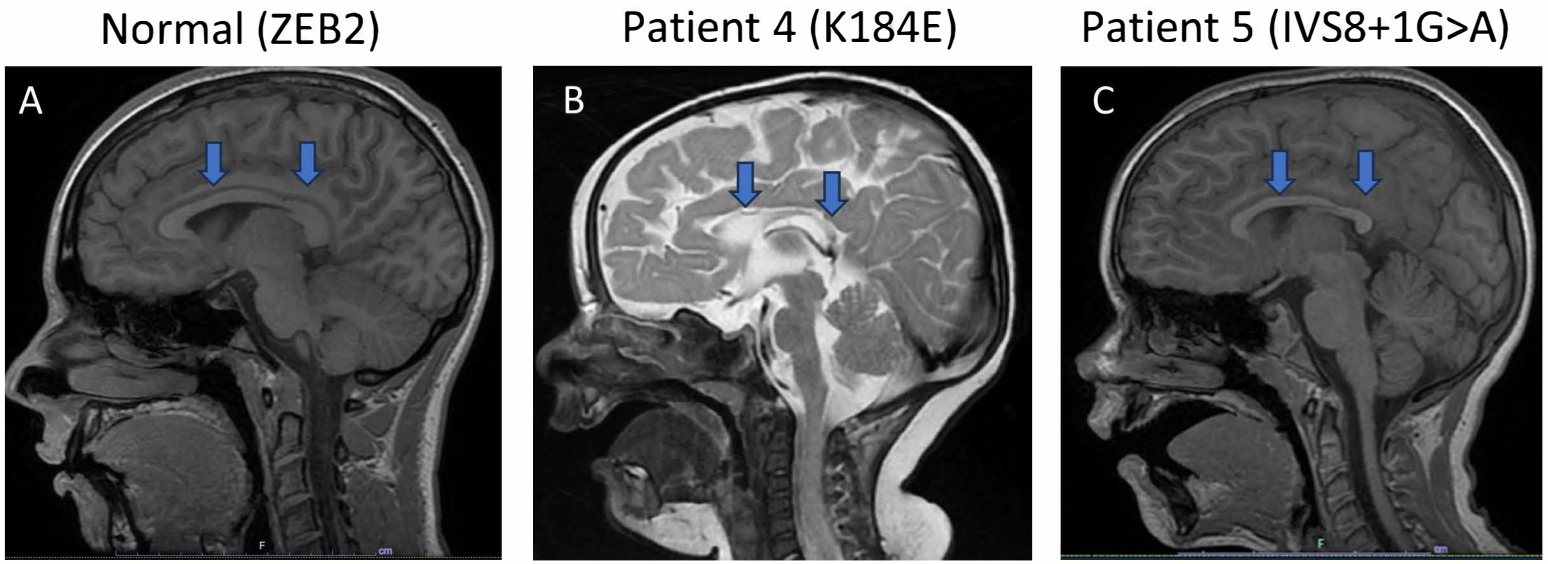

medRxiv preprint doi: https://doi.org/10.1101/2024.06.27.24309417; this version posted July 1, 2024. The copyright holder for this preprint (which was not certified by peer review) is the author/funder, who has granted medRxiv a license to display the preprint in perpetuity. It is made available under a CC-BY 4.0 International license .

Supplemental File 1. Survey for Patient Data Collection

We collected information about patients with known variants through an email survey to their providers. The following questions were included in the survey. Variant information was provided separately.

1) How was the genetics done? (i.e., Whole exome, panel on whole exome platform, whole genome, single gene sequencing)?
2) How old was the patient when diagnosed (with genetics)?
3) What is the patient's gender?
4) Does the patient have intellectual disability or developmental delay? If developmental delay: gross, fine or speech?
5) What growth changes are observed? (Delayed? Normal? Microcephaly? Macrocephaly?)
6) Does the patient have seizures? IF so, do you know the type?
7) Does the patient have congenital heart abnormalities? If yes, what type?
8) Has your patient had an MRI/A/S? If so, do you observe any of the following: Corpus collosum hypoplasia? Delayed myelination for age? Any malformations of brain?

Patient	1	2	3	4	5	6
TMEM184B nucleotide	c.262G>A	c.380T>G	C.484G>A	c.550A>G	c.787+1G>A	c.863G>C
Inheritance	De Novo	De Novo	De Novo	De Novo	De Novo	De Novo
Allele Frequency	0.000029	Not in gnomAD	Not in gnomAD	Not in gnomAD	Not in gnomAD	Not in gnomAD
Predicted Protein Alt	V88M	L127R	G162R	K184E	possibile loss of TM5 and most of TM6 and truncation after C263	G288A
Birth						
Sex	Female	Male	Female	Male	Female	Male
Age Of Onset						
General						
Gastrointestinal						
Respiratory						
Orthopedic / Craniofacial						
Neurological						
If Seizures, onset and						
Renal/Genito-urinary						
Cardiac						
Hematological						
Other Genetic Alterations						

Detailed clinical information has been removed in accordance with medRxiv policies. Please contact the corresponding authors to request access to these data.

Supplemental File 2

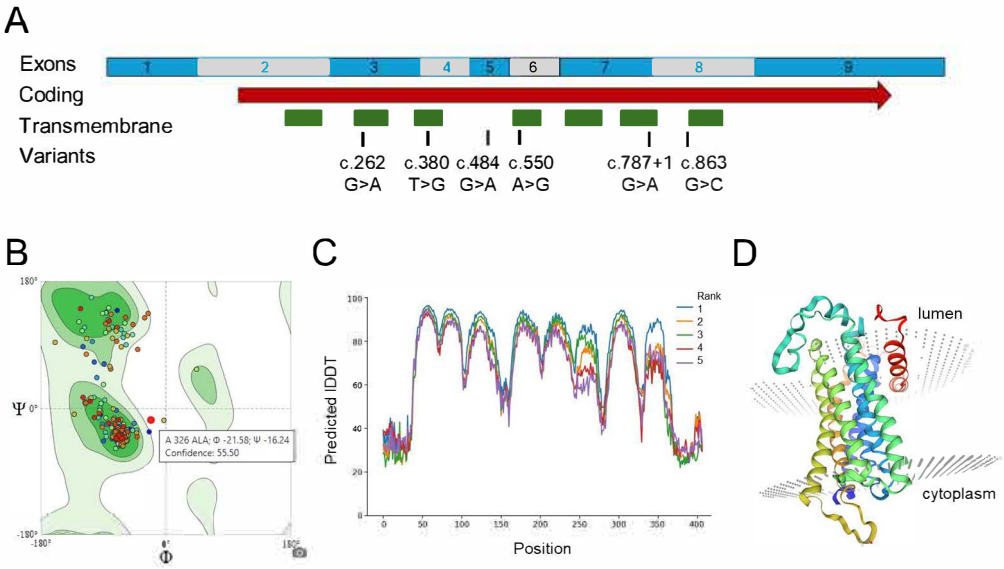

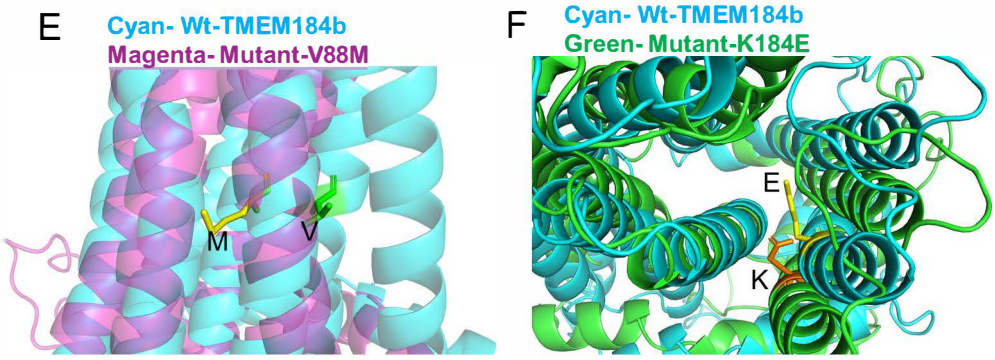

G

Variant	ΔG	ΔΔG (native)
Wild Type	477.51	NA
R282H	481.56	4.05
V88M	465.14	-12.37
L127R	493.69	16.18
G162R	467.43	-10.08
K184E	455.72	-21.79
G288A	491.35	13.84

H

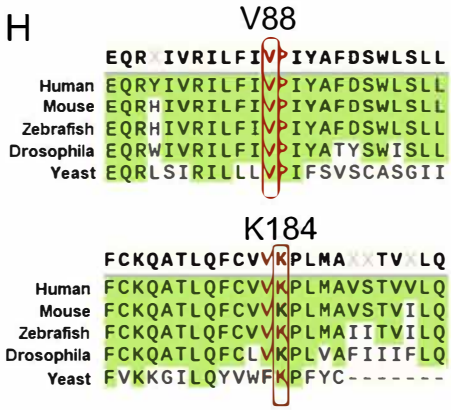

Figure 2

medRxiv preprint doi: https://doi.org/10.1101/2024.06.27.24309417; this version posted July 1, 2024. The copyright holder for this preprint (which was not certified by peer review) is the author/funder, who has granted medRxiv a license to display the preprint in perpetuity. It is made available under a CC-BY 4.0 International license .

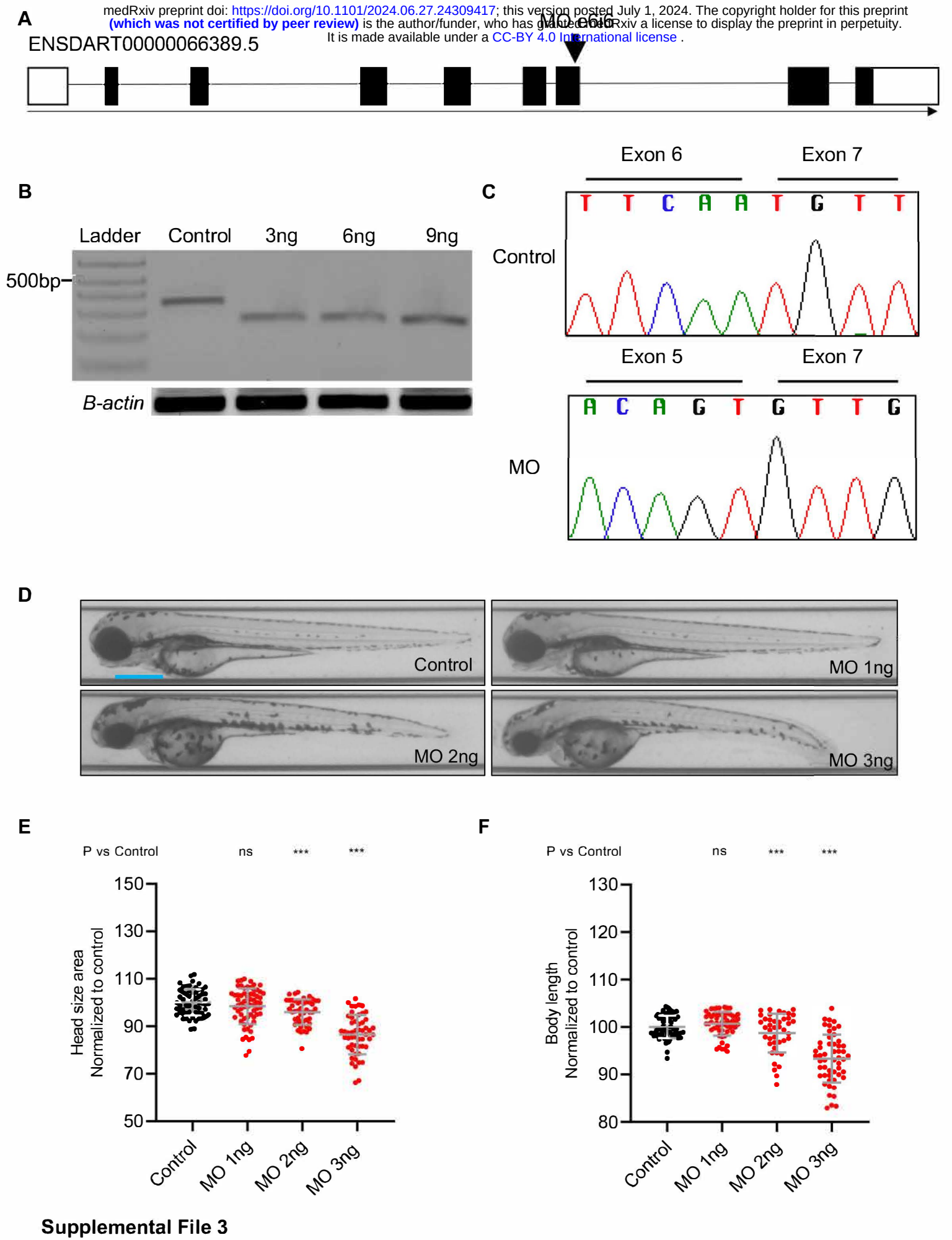

Supplemental File 3

medRxiv preprint doi: https://doi.org/10.1101/2024.06.27.24309417; this version posted July 1, 2024. The copyright holder for this preprint (which was not certified by peer review) is the author/funder, who has granted medRxiv a license to display the preprint in perpetuity. It is made available under a CC-BY 4.0 International license .

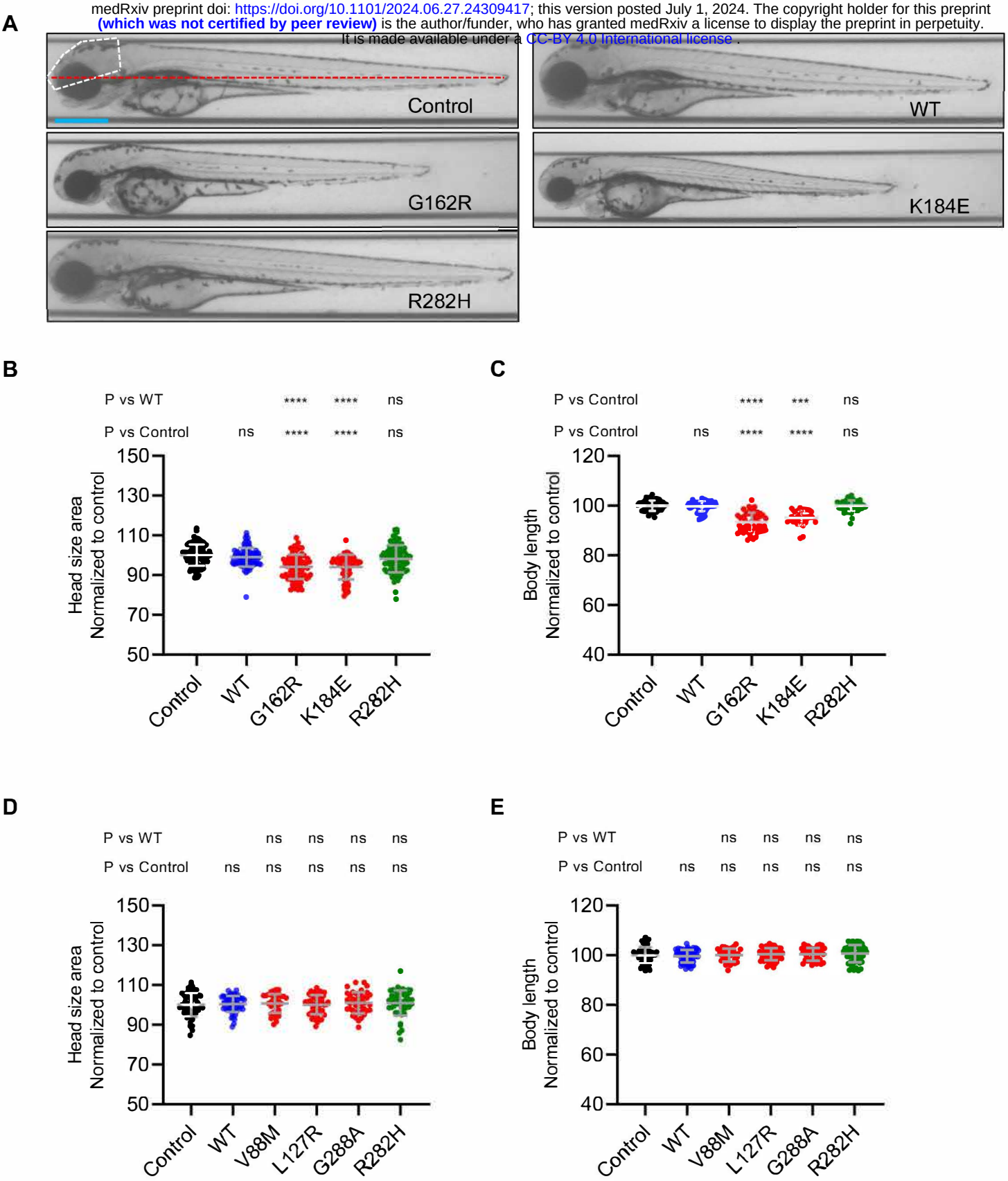

Figure 3

medRxiv preprint doi: https://doi.org/10.1101/2024.06.27.24309417; this version posted July 1, 2024. The copyright holder for this preprint (which was not certified by peer review) is the author/funder, who has granted medRxiv a license to display the preprint in perpetuity. It is made available under a CC-BY 4.0 International license.

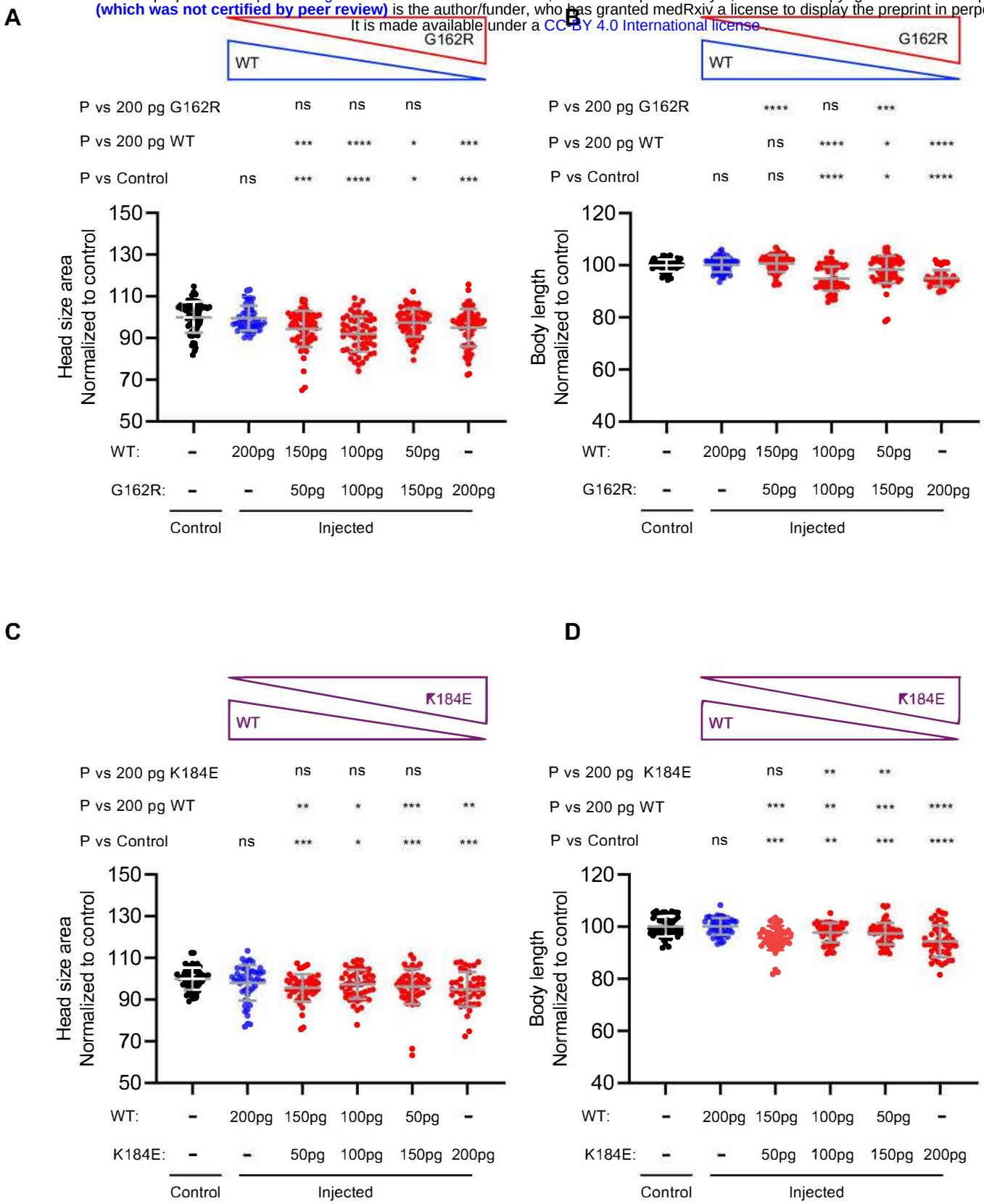

Figure 4

medRxiv preprint doi: https://doi.org/10.1101/2024.06.27.24309417; this version posted July 1, 2024. The copyright holder for this preprint (which was not certified by peer review) is the author/funder, who has granted medRxiv a license to display the preprint in perpetuity. It is made available under a CC-BY 4.0 International license .

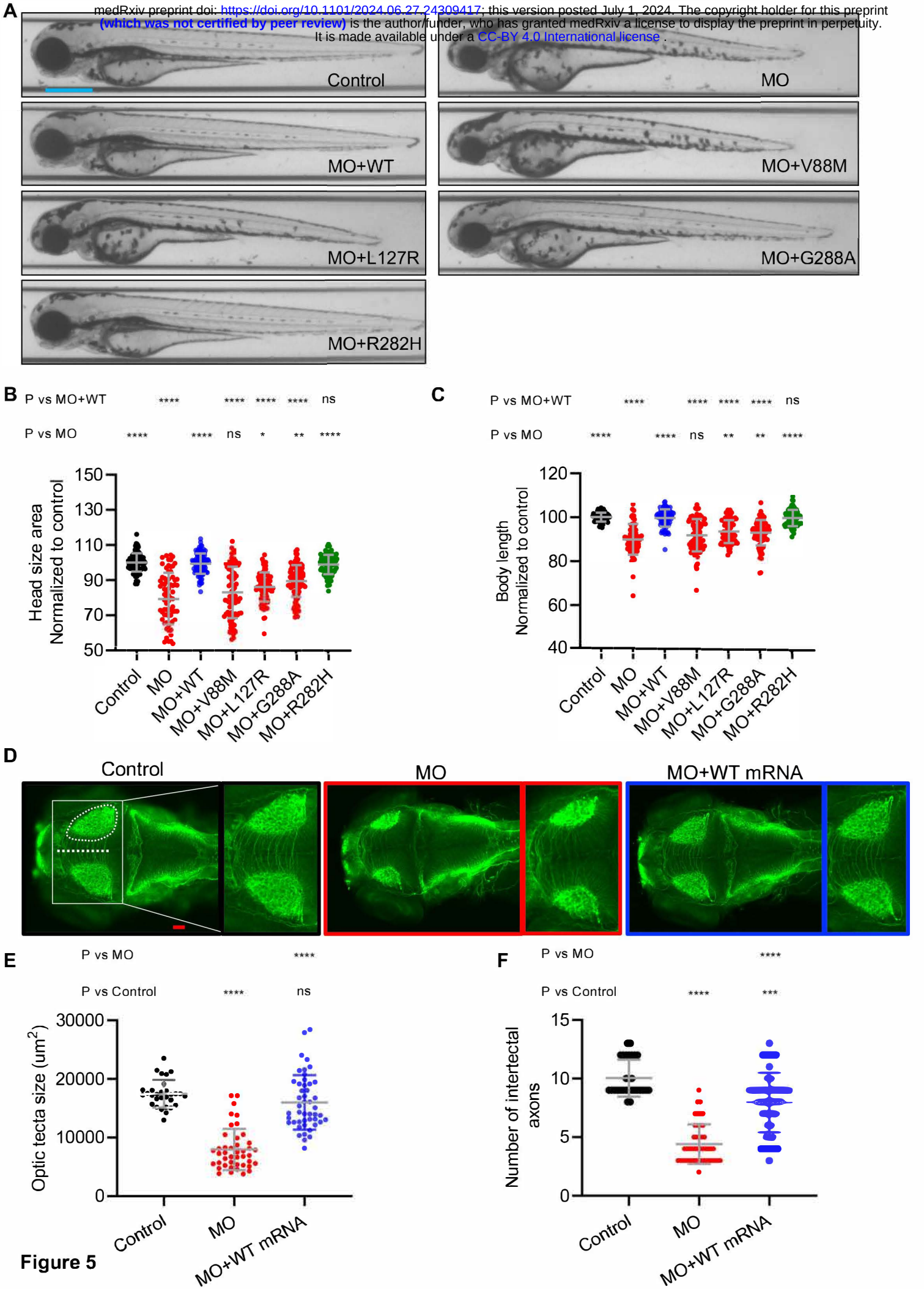

Figure 5

A

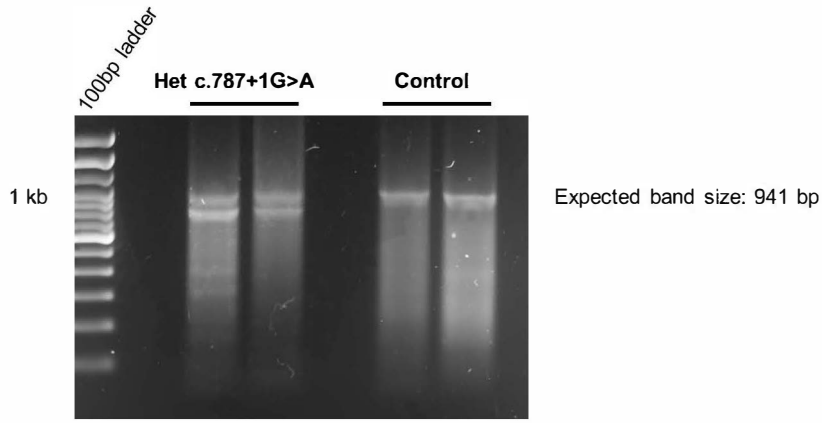

B

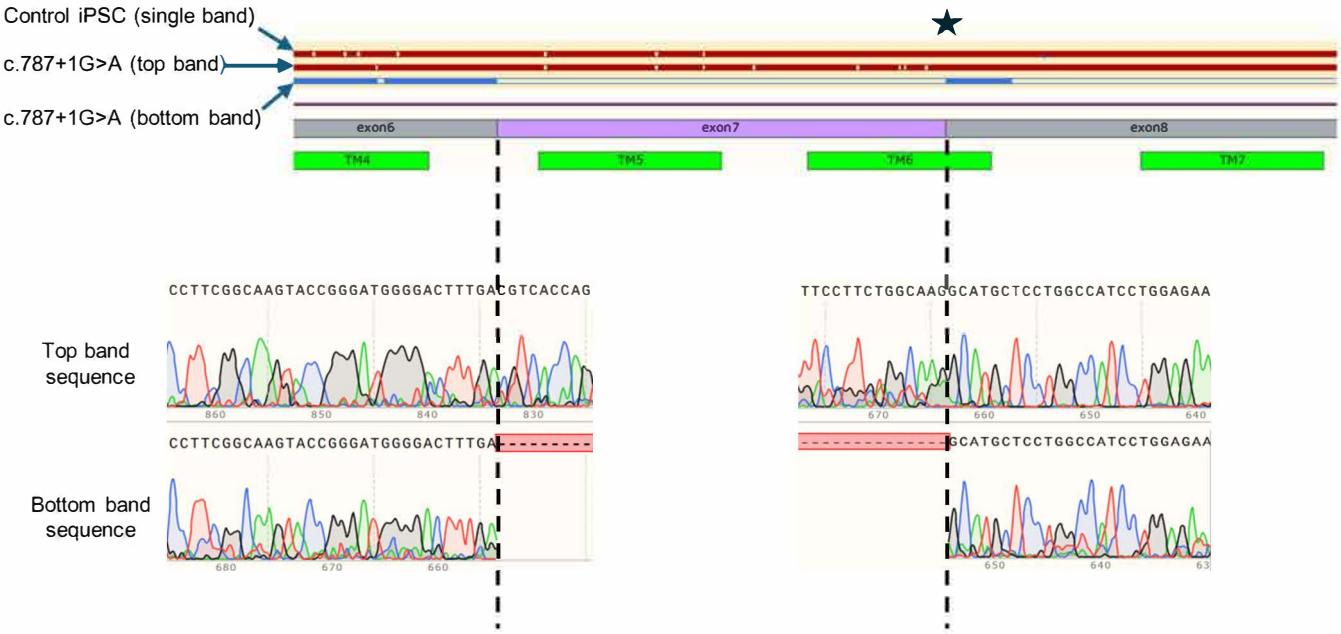

Supplemental File 4

medRxiv preprint doi: https://doi.org/10.1101/2024.06.27.24309417; this version posted July 1, 2024. The copyright holder for this preprint (which was not certified by peer review) is the author/funder, who has granted medRxiv a license to display the preprint in perpetuity. It is made available under a CC-BY 4.0 International license.

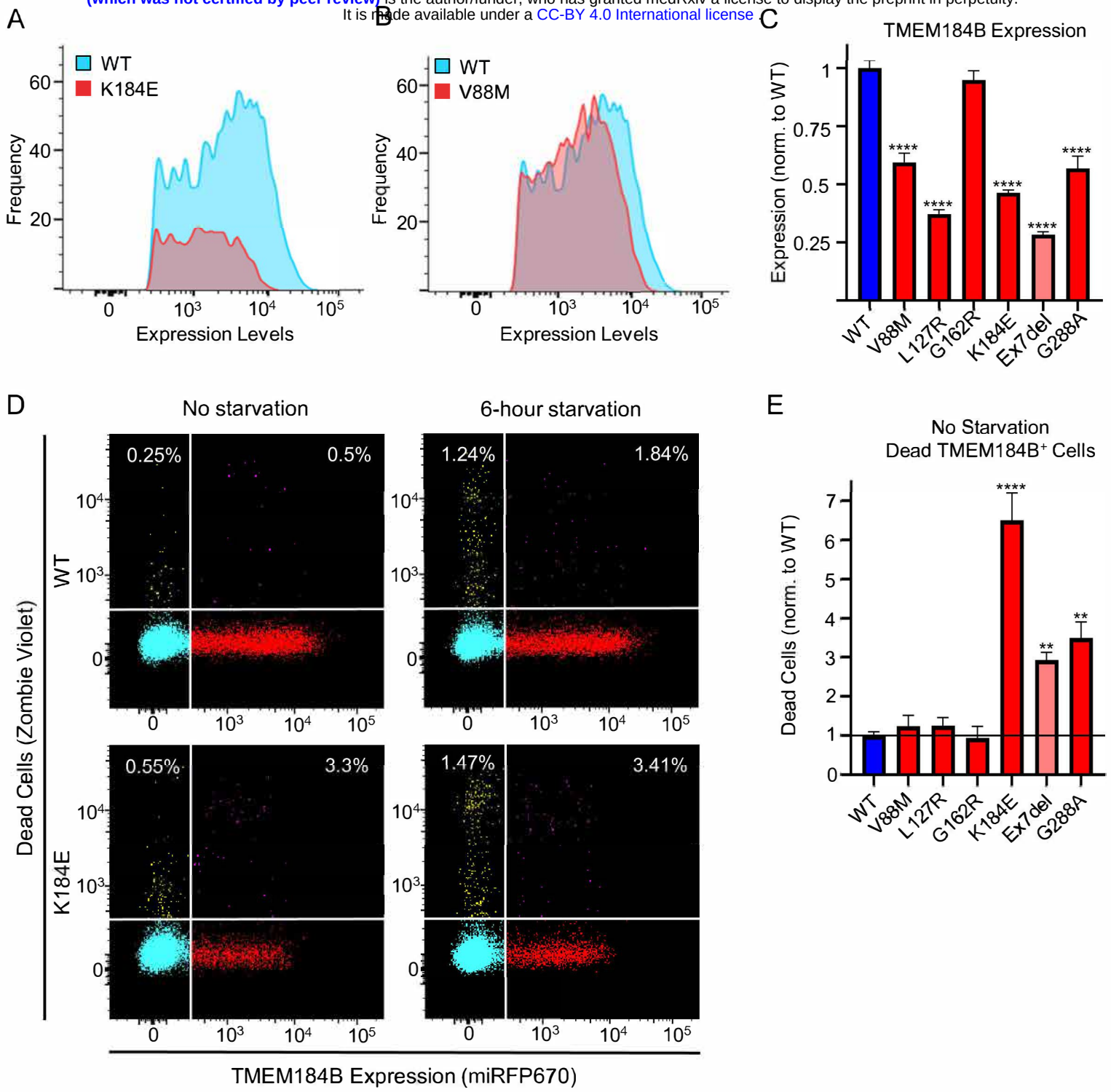

Figure 6

medRxiv preprint doi: https://doi.org/10.1101/2024.06.27.24309417; this version posted July 1, 2024. The copyright holder for this preprint (which was not certified by peer review) is the author/funder, who has granted medRxiv a license to display the preprint in perpetuity. It is made available under a CC-BY 4.0 International license .

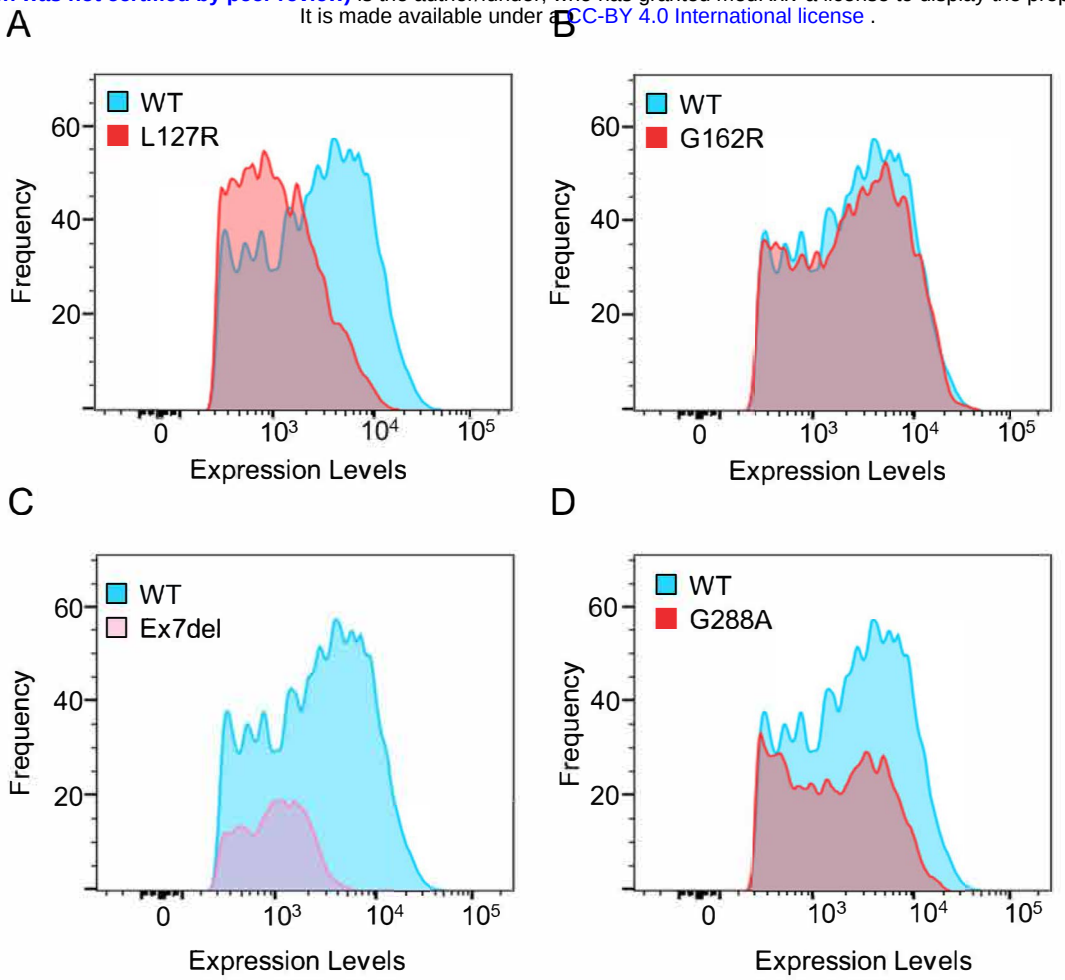

Supplemental File 5

medRxiv preprint doi: https://doi.org/10.1101/2024.06.27.24309417; this version posted July 1, 2024. The copyright holder for this preprint (which was not certified by peer review) is the author/funder, who has granted medRxiv a license to display the preprint in perpetuity. It is made available under a CC-BY 4.0 International license .

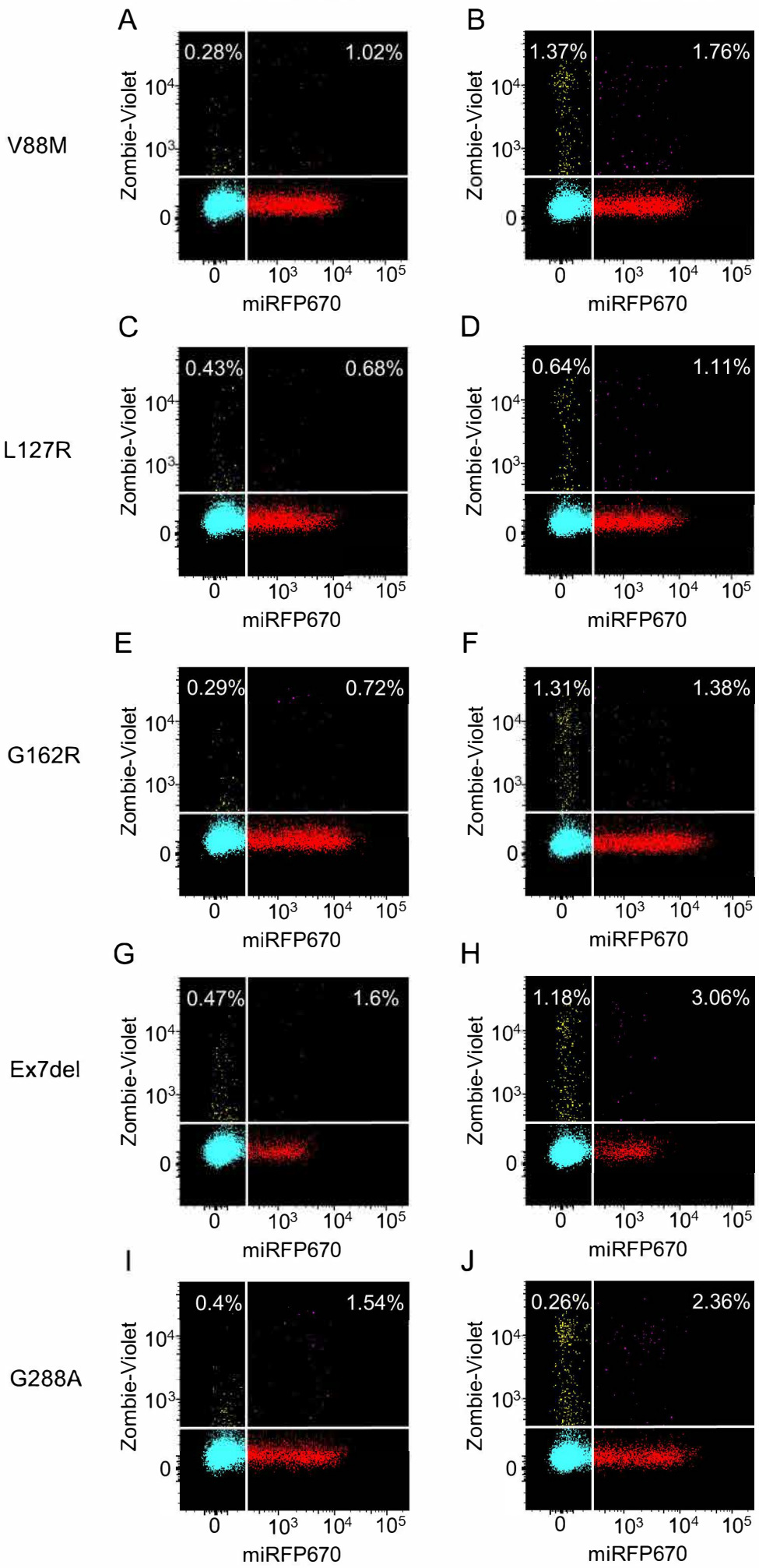

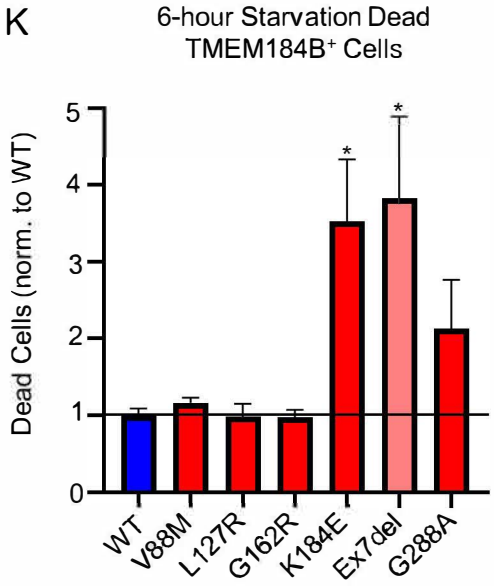

Supplemental File 6

medRxiv preprint doi: https://doi.org/10.1101/2024.06.27.24309417; this version posted July 1, 2024. The copyright holder for this preprint (which was not certified by peer review) is the author/funder, who has granted medRxiv a license to display the preprint in perpetuity. It is made available under a CC-BY 4.0 International license .

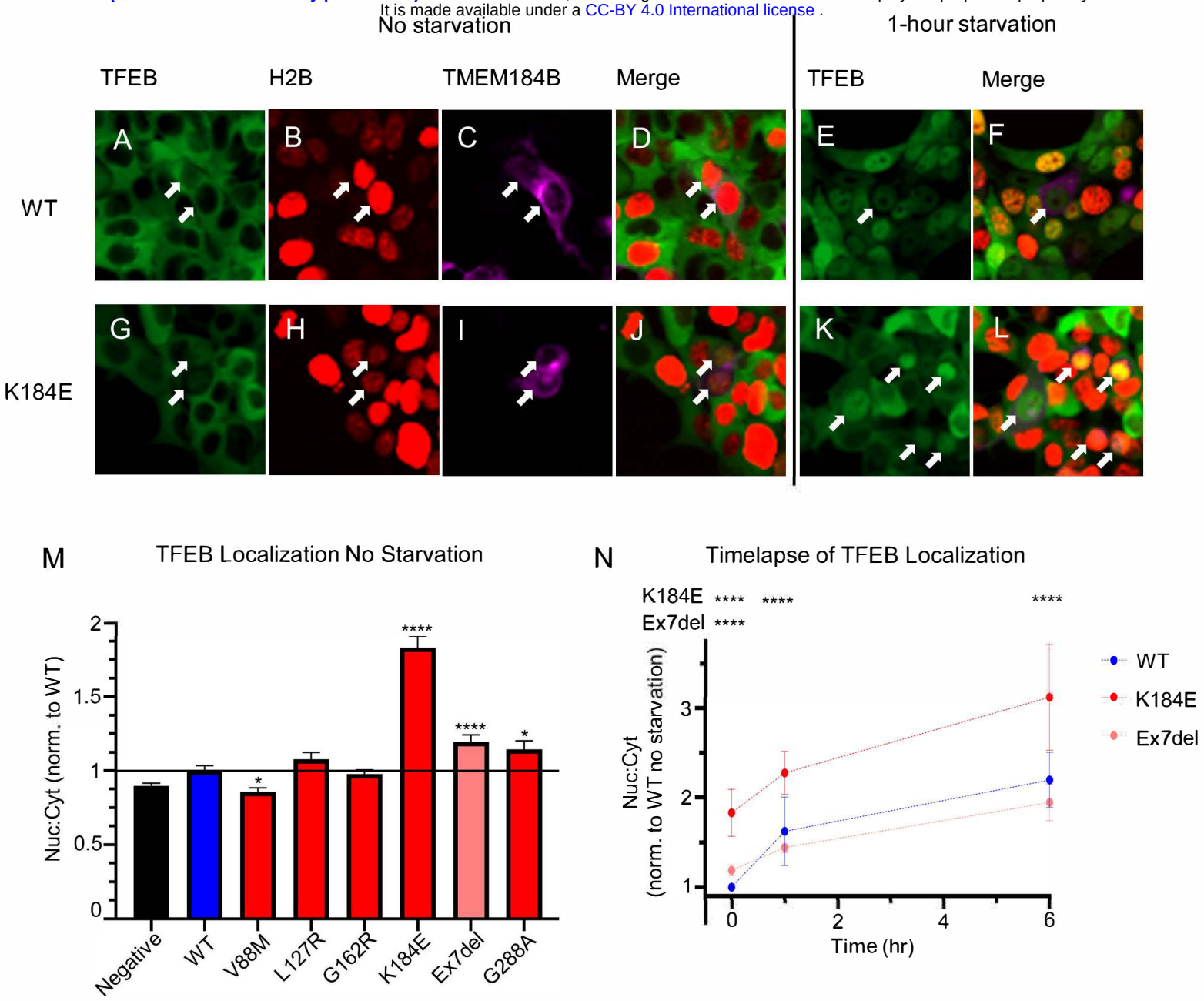

Figure 7

medRxiv preprint doi: https://doi.org/10.1101/2024.06.27.24309417; this version posted July 1, 2024. The copyright holder for this preprint (which was not certified by peer review) is the author/funder, who has granted medRxiv a license to display the preprint in perpetuity. It is made available under a CC-BY-4.0 International license.

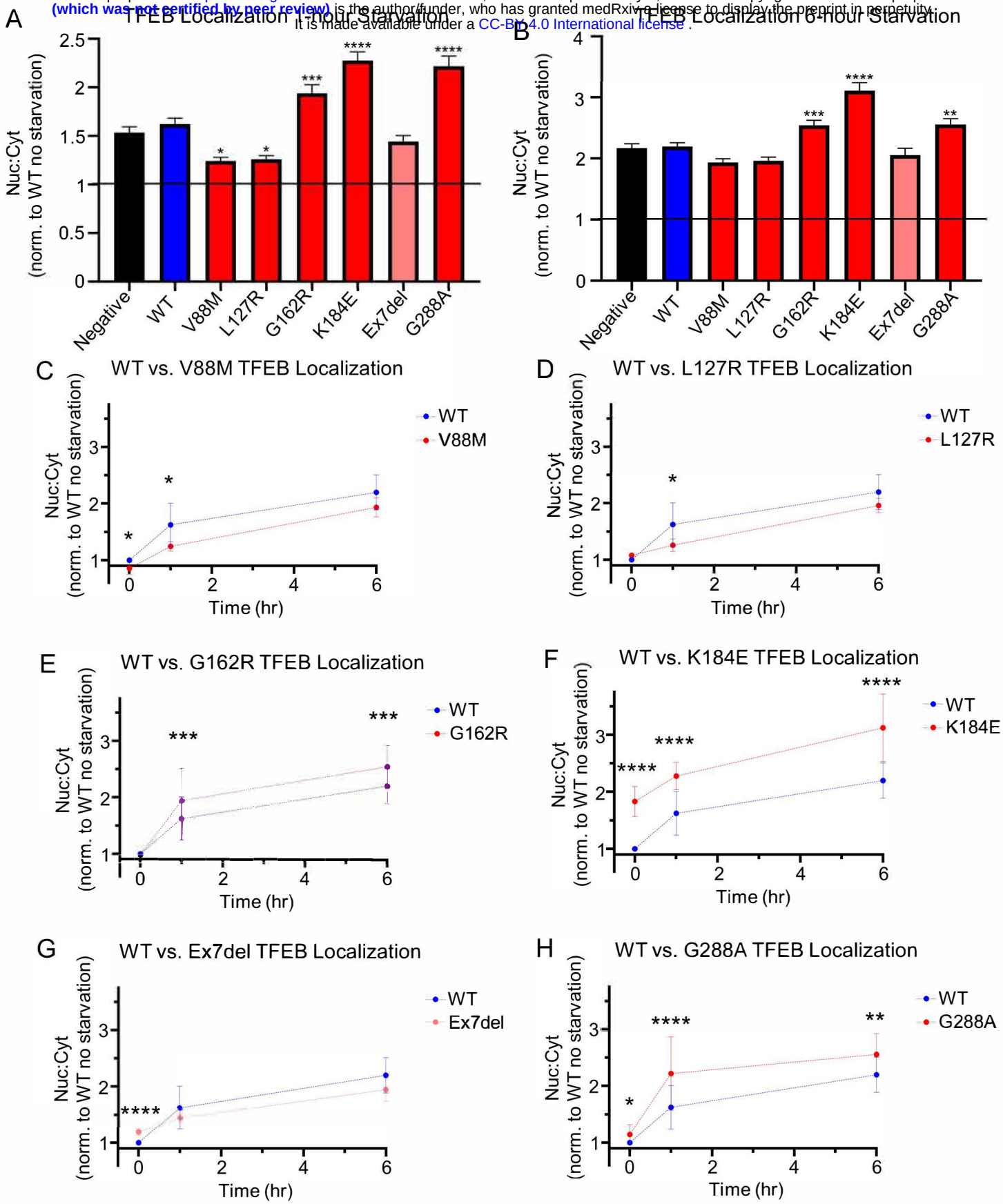

I

Patient	Variant	TFEB N:C No Starvation	TFEB N:C 1hr-Starvation	TFEB N:C 6hr-Starvation
1	V88M	*	*	
2	L127R		*	
3	G162R		***	***
4	K184E	****	****	****
5	IVS8+1G>A	****		
6	G288A	*	****	**

Supple-mentary File 7

medRxiv preprint doi: https://doi.org/10.1101/2024.06.27.24309417; this version posted July 1, 2024. The copyright holder for this preprint (which was not certified by peer review) is the author/funder, who has granted medRxiv a license to display the preprint in perpetuity. It is made available under a CC-BY 4.0 International license .

Protein Variant	DD/ID	Micro-cephaly	HCC	Seizures	ZF DN or Toxic	ZF Haplo-insufficient	Nuclear TFEB	Cell Death	ΔΔG
V88M					No	Yes	Down	Normal	Hyperstablized
L127R					No	Yes	Var	Normal	Destabilized
G162R					Yes	ND	Var	Normal	Hyperstablized
K184E					Yes	ND	Up	Up	Hyperstablized
IVS8+1G>A					ND	ND	Up	Up	ND
G288A					No	Yes	Up	Up	Destabilized

Var: had some effects but not statistically significant across all timepoints

Detailed clinical information has been removed in accordance with medRxiv policies. Please contact the corresponding authors to request access to these data.

Table 2